



HAL
open science

Lithosphere rigidity by adjoint-based inversion of interseismic GPS data, application to the Western United States

Severine Furst, Michel Peyret, Jean Chery, Bijan Mohammadi

► **To cite this version:**

Severine Furst, Michel Peyret, Jean Chery, Bijan Mohammadi. Lithosphere rigidity by adjoint-based inversion of interseismic GPS data, application to the Western United States. *Tectonophysics*, 2018, 746, pp.364-383. 10.1016/j.tecto.2017.03.015 . hal-01505024

HAL Id: hal-01505024

<https://hal.science/hal-01505024>

Submitted on 10 Apr 2017

HAL is a multi-disciplinary open access archive for the deposit and dissemination of scientific research documents, whether they are published or not. The documents may come from teaching and research institutions in France or abroad, or from public or private research centers.

L'archive ouverte pluridisciplinaire **HAL**, est destinée au dépôt et à la diffusion de documents scientifiques de niveau recherche, publiés ou non, émanant des établissements d'enseignement et de recherche français ou étrangers, des laboratoires publics ou privés.

Copyright

1 **LITHOSPHERE RIGIDITY BY ADJOINT-BASED INVERSION OF INTERSEISMIC**
2 **GPS DATA, APPLICATION TO THE WESTERN UNITED STATES**

3
4 Severine Furst^{a,*}, Michel Peyret^a, Jean Chéry^a, Bijan Mohammadi^b

5 ^a *Géosciences Montpellier, Université de Montpellier, CNRS UMR-5243, 34095 Montpellier, France*

6 ^b *IMAG, Université de Montpellier, CNRS UMR-5149, 34095 Montpellier, France*

7 *Corresponding author. *Email address:* severine.furst@gm.univ-montp2.fr S. Furst

8
9 **ABSTRACT**

10 While vertical motion induced by long-term geological loads is often used to estimate the
11 flexural rigidity of the lithosphere, we intend to evaluate the shear rigidity of the lithosphere
12 using horizontal motion. Our approach considers that the rigidity of the lithosphere may be
13 defined as its resistance to horizontal tectonic lateral forces. In this case, a spatial distribution
14 of an effective shear rigidity can be estimated from the analysis of the interseismic velocity
15 fields. We consider the Western United States zone where weakly strained areas (e.g., the
16 Sierra Nevada) are connected with areas of large strain rate (e.g. San Andreas Fault system).
17 By inverting interseismic strain distribution measured by geodetic methods, we infer the
18 effective shear rigidity of the lithosphere. The forward problem is defined using the equations
19 of linear elasticity. The inversion relies on the minimization of the sum of a quadratic measure
20 of the differences between measured and modelled velocity fields. The functional also
21 includes regularization terms for the parameters of the model. The gradient of the functional
22 with respect to the minimization parameters is computed using an adjoint formulation. This
23 permits the treatment of large dimensional minimization problems. Finally, a measure of the
24 uncertainty of our inversion is illustrated through the covariance matrix of the parameters at
25 the optimum. The optimization chart is validated on two synthetic velocity distributions.

26 Then, the effective shear rigidity variations of the Western United States are estimated using
27 the CMM3 interseismic velocities. The inversion displays low effective rigidities along the
28 San Andreas Fault system, the Mojave Desert and in the Eastern California Shear Zone, while
29 rigid areas are found in the Sierra Nevada and in the South Basin and Range. Finally, we
30 discuss the differences between our strain rate and rigidity maps with previously published
31 results for the Western United States.

32

33 *Keywords: GPS; interseismic velocity; effective rigidity; global optimization; San Andreas*
34 *Fault system; uncertainties.*

35

36 **1. INTRODUCTION**

37 Geological strain occurring over millions of years results from the continuous accumulation
38 of anelastic processes in the crust and in the lithosphere in response to plate motion. Active
39 deformation areas are identified by seismicity and geodetic deformation. In active
40 deformation area, the comparison of plates motion from geology and geodesy, at these two
41 different time scales, provides a fair agreement in term of horizontal velocities (Sella et al.,
42 2002). Geologic and geodetic comparisons can also be made across active faults using
43 standard models for interseismic strain (McCaffrey, 2005; Meade and Hager, 2005; Savage
44 and Burford, 1973). It appears that most of the documented faults display a close agreement
45 between geodetic and geologic strain rates (Vernant, 2015).

46 From a mechanical viewpoint, the close agreement between short and long-term strain rates
47 (i.e. time scales from 10 yrs to 1 Myrs) probably reflects the stability of the stress balance in
48 the lithosphere under the action of slowly evolving remote forces associated to subduction,
49 basal drag and, more generally, the plate system gravitational potential energy. Under the
50 action of these forces, strain distribution is mostly controlled by the lithospheric strength. By

51 strength we mean the maximum force sustainable by the lithosphere. Like lithospheric stress,
52 lithospheric strength cannot be determined precisely with depth, unless with crude rheological
53 yield strength envelope models (Tesauro et al., 2011). Indeed, a precise strength estimate with
54 depth would require a detailed knowledge of the temperature profile with depth, lithology and
55 water contents, as well as friction law in the brittle domain and temperature dependent viscous
56 laws in the ductile crust and mantle. Therefore, the lithospheric strength can only be
57 approached through its integral measure along depth, with numerical models of the
58 lithosphere. These solve stress equilibrium using elasto-visco-plastic laws with prescribed
59 boundary conditions (Bird and Kong, 1994; Chéry et al., 2001). However, a simplified
60 version of lithospheric strength is embedded in the concept of effective elastic thickness
61 (EET) applied to plate flexure. Indeed, it has been shown that plates submitted to topographic
62 and other internal loads display vertical motions controlled by plate rigidity (Watts, 2001).
63 Combined analysis of topographic and gravimetric signals allows for computing effective
64 elastic thickness and its variation at continental scale (Lowry and Smith, 1994; Pérez-
65 Gussinyé et al., 2009). A fair agreement is generally found between heat flow and EET where
66 small values of EET correspond to high heat flow zones.

67 Both lithospheric strength and effective elastic thickness are commonly associated with the
68 long-term behaviour of the lithosphere. However, these concepts can be adapted in order to
69 interpret interseismic geodetic measurements (Chéry, 2008). For a typical time of 10 years of
70 geodetic observation and in the absence of large earthquakes, a linear evolution of GPS
71 motion is often observed. Therefore, a collection of GPS velocities may be used in order to
72 compute strain rate maps at plate scale (Kreemer et al., 2014). Even if this latter analysis is
73 purely kinematic, the resulting geodetic strain rate must satisfy stress equilibrium over the
74 time of observation. In such a problem, the unknown is the incremental lithospheric strength.
75 One example is the spatial variation of the stress change integrated over the depth over the

76 time of GPS observation. The problem can be simplified assuming that lateral strength
77 variation is modulated by geodetic plate thickness (Chéry, 2008). The integrated value of the
78 shear-stress at depth is what we call the effective shear rigidity. It is conceptually similar to
79 the flexural rigidity: the effective shear rigidity expresses the resistance of the lithosphere to
80 lateral forces (unit is N), while the effective flexural rigidity is related to the resistance of the
81 lithosphere to vertical bending (unit is N.m).

82 In Chéry et al. (2011), we proposed a global optimization approach to estimate effective plate
83 rigidity maps by the inversion of a GPS velocity field. The inversion provides a rigidity field
84 realizing a RMS between the observed and modelled velocity fields close to 2 mm/yr for a
85 dataset in southern California. However, we faced difficulties to properly fit high velocity
86 gradients in the vicinity of the San Andreas Fault system. This is because the method did not
87 allow the consideration of large inversion problem and therefore the local spatial density of
88 our model parameters was too low. Moreover, a priori velocity boundary conditions were
89 necessary and no uncertainties estimated.

90 In this paper, we present an enhanced version of the method to address the previous issues:

- 91 • the number of optimization variables can now be arbitrary thanks to the use of an
92 adjoint formulation of the forward problem. This permits high spatial resolution for
93 the rigidity.
- 94 • boundary conditions are not anymore prescribed but now treated as optimization
95 variables as well.
- 96 • uncertainties are calculated for optimal rigidity value.

97 The paper is organized as follows: (1) we describe the new features of the method and we
98 state the differences with respect to Chéry et al. (2011), (2) we demonstrate the efficiency of
99 our new approach on a synthetic dataset that mimics a strike slip fault locked at depth, (3) we
100 propose a refined rigidity map of southern California and we study the sensitivity of the

101 solution of the inversion problem with respect to the location of domain boundaries. Finally,
102 (4) we compare and discuss our results with those already published, both in terms of strain
103 rate maps and effective elastic thickness.

104

105 **2. GOVERNING EQUATIONS AND FORWARD MODELLING**

106 Geophysical laws provide the mathematical framework to compute the outcome of some
107 physical processes: this is called the forward problem. In other words, the model and its inputs
108 are known and specific data (e.g. seismic, geodetic, or magnetic) are sought thanks to the
109 equations linking the physical parameters to the solution at the observation location. Most of
110 the time, we only have access to the consequences of a physical process (e.g. the geodetic
111 measurements). These consequences need to be inverted to determine the physical properties
112 of the Earth interior (Tomography: e.g. Montelli et al., 2004; Tanaka et al., 2009. Volcanoes
113 and geothermal zones: e.g.; Anderson and Segall, 2013; Dzurisin, 2003; Mossop and Segall,
114 1999. Application to reservoirs: e.g. Hesse and Stadler, 2014). In some cases, there are
115 analytical theories dictating the distribution of model's parameters that accurately reproduces
116 the observations. For most geophysical problems, the limited amount of data used to
117 reconstruct a model with infinite degrees of freedom leads to the non-uniqueness of the
118 solution. Consequently, the inverse problem only provides one of the many models that
119 explain the data and has uncertainty because the real data are subject to uncertainties and
120 errors.

121 The effective elastic thickness of the lithosphere can vary laterally due to both elastic
122 properties and the rheological failure properties that limit elastic strength. Flow strength
123 depends on other factors than the temperature. Also, part of the variation imaged by the
124 geodetic technique is probably due to the limits of frictional strength on faults (Bird and
125 Kong, 1994). The thermal plate regime probably exerts a large influence due to the sensitivity
126 of the effective plate rigidity with respect to its temperature profile (Watts, 2001). Here, we

127 model these rigidity variations as lateral variations of the elastic properties of a plate with
 128 constant thickness. Thus, our forward model is made of a domain (Ω) symbolizing a 2-D
 129 plate, which can deform according to linear and isotropic elasticity (Fig. 1). Along the
 130 boundary of the domain $\partial\Omega$, we apply Dirichlet conditions (i.e., in-plane velocities u_{BC}) and
 131 assume free normal traction at the surface of the plate (plane stress assumption). This
 132 hypothesis means that strain perpendicular to the plane can occur. The forward model is
 133 therefore composed of three equations, the stress equilibrium (Eq. 1), a constitutive equation
 134 linking the strain rate to the stress rate for a 2-D plate (Eq. 2) and boundary conditions (Eq.
 135 3):

$$\text{div}(\dot{\sigma}) = 0 \quad \text{on } \Omega \quad (1)$$

$$\dot{\sigma}_{ij} = \frac{E(x, y)}{1 + \nu} \left(\dot{\varepsilon}_{ij} + \frac{\nu}{1 - 2\nu} \dot{\varepsilon}_{kk} \delta_{ij} \right) \quad \text{on } \Omega \quad (2)$$

$$u = u_{BC} \quad \text{on } \partial\Omega \quad (3)$$

136 where $\dot{\varepsilon}$ and $\dot{\sigma}$ are the strain- and stress-rate tensors, δ is the Kronecker delta function, i, j and
 137 $k = 1, 2$. Because of the relatively small variation of the Poisson's ratio for the lithosphere, ν
 138 is assumed to be constant and equal to 0.25. The Young modulus E remains the only free
 139 mechanical parameter in this equation. Since the model is driven by a velocity condition, only
 140 the relative variation of the Young's modulus matters for strain computation. This means that
 141 any distribution of the form $C \times E(x, y)$ provides the same velocity field
 142 u regardless the value of the constant C . For this reason, we define the non-dimensional
 143 effective rigidity distribution $D(x, y)$ as $\frac{E(x, y)}{E_{min}}$ where E_{min} is the minimum value of $E(x, y)$
 144 over the domain. So, all distributions of D presented in this paper range from 1 to some
 145 maximum values.

146 For a given spatial domain, we generate a uniform 2-D Delaunay mesh composed by
 147 triangles. In order to estimate the velocity field u at geodetic measurement locations we use

148 the academic 2-dimensional finite element code CAMEF. The code does not incorporate the
 149 value of the plate thickness. Therefore, we cannot discriminate plate thickness and elastic
 150 properties of the lithosphere from the rigidity values. Hence, fixing an absolute value to the
 151 rigidity remains an open problem. Finally, the velocity field u produced by the forward model
 152 depends on two input parameter sets: the velocity boundary conditions u_{BC} and the
 153 distribution of $D(x, y)$ (Fig. 1). Eventually, we try to fit u with the observations u^* .

154

155 **3. INVERSION METHOD**

156 Running the direct problem requires the prescription of the velocity on the boundary nodes
 157 and the rigidity for each mesh element. Contrary to the approach proposed in Chéry et al.
 158 (2011), the boundary conditions are not imposed anymore in the inverse problem and are
 159 treated as optimization parameters. We associate one rigidity parameter to each mesh element
 160 leading to a very large optimization problem. Our global optimization algorithm requires the
 161 gradient of the functional. We consider an adjoint formulation of the forward model to access
 162 this gradient with respect to all the model parameters simultaneously.

163 **3.1 Cost function**

164 We want to invert observed data u^* and determine the model parameters $p(D, u_{BC})$
 165 minimizing the distance (here L_2 -norm) between the observed data u^* and the predicted field
 166 $u(p)$ inside the domain Ω :

$$J(p) = \|u^* - u(p)\|_{\sigma^{-1}}^2 \quad (4)$$

167 where J is the cost function to minimize, and subscript σ^{-1} means that the L_2 -norm is
 168 weighted by the inverse of the covariance matrix of the geodetic measurements.

169 Geophysical inverse problems are usually ill-posed and need to include a subjective degree of
 170 regularisation to achieve relevant geophysical solutions (e.g. Zaroli et al., 2013). We therefore
 171 introduce to the cost function two Tikhonov regularization terms to control local fluctuations

172 of the parameter vector (Tarantola, 2004; Tikhonov, 1943). We separate the regularization of
 173 the parameters along the boundaries u_{BC} and those associated to the rigidity D inside the
 174 domain:

$$J(p) = \|u^* - u(p)\|_{\sigma^{-1}}^2 + \lambda_1 R_1(D) + \lambda_2 R_2(u_{BC}) \quad (5)$$

175 where $R_1(D)$ and $R_2(u_{BC})$ are regularization operators. The former acts over the domain and
 176 controls the regularity of the rigidity distribution, while the latter monitors the regularity of
 177 the boundary conditions. Both are particular forms of non-linear Laplace-Beltrami operators
 178 with a local control of the level of regularization (Mohammadi and Pironneau, 2009). The
 179 weights λ_i have to be chosen by the user. Series of different optimizations have been run to
 180 highlight the effect of λ_i on the inversion. By doing so, our goal is to adjust $u(p)$ to the data
 181 u^* , while preserving some degree of regularity on both the rigidity inside the domain and the
 182 velocities along the boundaries. However, for each simulation, we only have the values of the
 183 velocities (and not rigidity) to compare with. Hence, adjusting the regularity of the rigidity is
 184 largely subjective and we found that using no regularization ($\lambda_1 = 0$) for rigidity leads to
 185 acceptable spatial rigidity gradients. Hence, in this study, we only consider the regularization
 186 term of the boundary conditions.

187 In order to choose λ_2 , we explore the *trade-off* between the residual data misfit $Res(p) =$
 188 $\|u^* - u(p)\|^2$ and the regularization term $R_2(u_{BC})$. This is featured in a *trade-off* or Pareto
 189 curve, which gathers all feasible solutions that cannot be improved in any of the objectives
 190 without degrading the other objectives (e.g. Vassilvitskii and Yannakakis, 2005). The
 191 selection of an optimally regularized solution depends upon the requirements of a particular
 192 study. We will illustrate the impact of the regularization over the boundary conditions for the
 193 rigidity inversion in Southern California.

3.2 Global optimization

We apply a global optimization algorithm (Ivorra et al., 2013) to iteratively invert interseismic geodetic data. Global optimization is necessary as we have no information on the convexity of the cost function and several local minima can be present. The global optimization strategy is meant to improve the initial condition for classical gradient-based methods looking for an initialization in the attraction basin of the global optimum (Mohammadi and Pironneau 2009). In addition to the Tikhonov regularization mentioned above, the gradient of the functional is smoothed (Mohammadi and Pironneau, 2004, 2009) in order to control the regularity of the parameters. The optimization algorithm ends when the functional or the variations of the gradient are smaller than some user-defined thresholds. A synthetic flow chart of the inverse problem is given in Fig. 2.

Functional derivatives computation is done using an adjoint formulation of the forward model (e.g. Plessix, 2006). In most of the inverse problems in geophysics, the cost function cannot be analytically linearized. If a finite difference approach is adopted, the number of forward computations for assessing the gradient of the functional is proportional to the number of parameters. Let us briefly recall the adjoint technique. The gradient of the functional with respect to the model parameters can be expressed as follows:

$$\nabla_p J = \frac{\partial J}{\partial p} + \left(\frac{\partial J^t}{\partial u} \frac{\partial u}{\partial p} \right)^t \quad (6)$$

where J is the functional, p the parameters and u the velocity calculated at each node of the mesh. From the equilibrium equation $\mathbf{K}u = f$, we incorporate the rigidity matrix \mathbf{K} and the stress vector f in (Eq. 6):

$$\nabla_p J = \frac{\partial J}{\partial p} + \left(\frac{\partial J^t}{\partial u} \cdot \mathbf{K}^{-1} \cdot \left(\frac{\partial f}{\partial p} - \frac{\partial \mathbf{K}}{\partial p} u \right) \right)^t \quad (7)$$

214 Defining the adjoint variable V as the solution of the system $\mathbf{K}^t \cdot V = \mathbf{K} \cdot V = \frac{\partial J}{\partial u}$ (because \mathbf{K} is
 215 self-adjoint in our case), we obtain:

$$\nabla_p J = \frac{\partial J}{\partial p} + \left(V^t \cdot \left(\frac{\partial f}{\partial p} - \frac{\partial \mathbf{K}}{\partial p} \cdot u \right) \right)^t \quad (8)$$

216 Consequently, the amount of computation needed to obtain the gradient of the functional
 217 mostly corresponds to the solution of one forward model, by opposition to a finite difference
 218 scheme which needs a number of forward model solutions equal to the number of parameters.

219 **3.3 Model Parameters initialization**

220 Real GPS datasets present large spatial variations of density measurements. GPS stations are
 221 usually set to observe the velocity gradient around fault zones. Therefore, we usually expect
 222 null strain in geographical areas where measurements are sparse. This information can be
 223 used to define the initial guess for the lithosphere rigidity in the optimization procedure. This
 224 is similar to what is done in topological optimization (e.g. Allaire et al., 2004) where the
 225 initial structural rigidity is set to the maximum admissible value. Optimization then aims at
 226 making the structure softer and softer. A common problem in mechanical structure design is
 227 to optimize the topology of an elastic structure given certain boundary conditions. Optimality
 228 implies to minimize the weight, but at the same time, the structure needs to be as strong and
 229 rigid as possible. The rigidity of each element is hence reduced at each iteration of
 230 optimization when requested.

231 Synthetic and real cases presented in this paper involve rigidity reaching very large values in
 232 areas that exhibit little internal deformation. Thus, the rigidity amplitude ranges from a given
 233 minimum to infinity in no-deformation zones. This semi-open variation domain is not suitable
 234 for numerical search. Consequently, we choose a parametrization design using the
 235 compliance, $C = \frac{1}{D}$, of the material instead of the rigidity. The compliance is defined over the

236 interval $[\varepsilon, 1]$, the lower bound corresponding to a quasi-rigid body. We have considered
 237 different values of ε . It appears that a value of $\varepsilon = 0.01$ which corresponds to two order of
 238 magnitude admissible variation for the rigidity is sufficient to fully capture the range of most
 239 strain-rates observed at the Earth's surface (see discussion in Appendix B). This use of
 240 compliance insures greater stability of the inversion process. For ease of understanding and
 241 interpretation, we express our results in terms of rigidity D after the inversion is completed.

242 **3.4 Model parameters uncertainty**

243 GPS observations are plagued with uncertainty due to various factors: instrumental noise,
 244 field measurement procedure, the skill of the operator and local environmental motions. These
 245 uncertainties affect in a complex way the GPS time series and generate a coloured noise on
 246 positions (Mao et al., 1999). But, these also induce uncertainties on the model parameters
 247 determined through our optimization process. For that reason, it is essential to quantify the
 248 impact of data uncertainty propagating through the inversion. Hence, the resulting rigidity
 249 distribution is complemented with a sensitivity map.

250 To determine the model parameters uncertainties, we link the covariance matrices of the
 251 parameters and data. Let us consider the observation u^* (geodetic velocities) as a sum of a
 252 'true and noise-free' value u_r with zero variance (i.e. $cov(u_r) = 0$) and an uncertain quantity
 253 δu : $u^* = u_r + \delta u$. For this sum, the covariance matrix is given by:

$$cov(u^*) = cov(u_r) + cov(\delta u) + 2cov(u_r, \delta u) \quad (9)$$

254 Because u_r is deterministic, u_r and δu are independent (i.e. $cov(u_r, \delta u) = 0$). Therefore, the
 255 covariance matrix reduces to:

$$cov(u^*) = cov(\delta u) \quad (10)$$

256 We consider a linear relationship between δp and δu :

$$\delta u = (\nabla_p u) \cdot \delta p \quad (11)$$

257 which leads to:

$$cov(u^*) = J.cov(\delta p).J^t \quad (12)$$

258 where $J = \nabla_p u$ is the Jacobian matrix made of the derivatives of the velocities at geodetic
 259 measurement locations with respect to the model parameters. Similarly to (Eq. 9), we define
 260 the covariance matrix of the predicted parameters $cov(p_{obs})$ as:

$$cov(p_{obs}) = cov(p_r) + cov(\delta p) + 2cov(p_r, \delta p) \quad (13)$$

261 where p_r (the actual values of the parameters) is assumed deterministic. Again, p_r and δp are
 262 assumed independent, and therefore:

$$cov(p_{obs}) = cov(\delta p) \quad (14)$$

263 Finally, equation (Eq. 12) becomes:

$$cov(u^*) = J.cov(p_{obs}).J^t \quad (15)$$

$$cov(p_{obs}) = J^{-1}.cov(u^*).J^{-t} \quad (16)$$

264 So, this equation formulates the uncertainty propagation from geodetic measurements to the
 265 model parameters via the Jacobian matrix J . The construction of this matrix can be performed
 266 in two different ways. The simplest approach consists in expressing it analytically as a
 267 function of the gradients that have been evaluated during the resolution of the adjoint
 268 problem. Indeed, J can be explicitly deduced from the equation $\nabla_p J = \frac{\partial J}{\partial p} + \left(\left(\frac{\partial J}{\partial u} \right)^t J \right)^t$. This
 269 approach is straightforward and theoretically correct, but it is numerically unstable since it
 270 involves the inversion of singular matrices. Consequently, it is more robust to build J from
 271 finite difference computations. This consists in perturbing one parameter around its
 272 optimum (typically by 10%), and then computing the perturbation of the predicted velocity at
 273 all geodetic measurement locations. This approach is numerically robust because it involves
 274 no matrix inversion. With the second member of Eq. 16 in hand, we can now provide an
 275 estimation of the variance (diagonal of the covariance matrix) of the optimization variables.

276 In this study the parameter is the compliance C with its standard deviation $dC =$
 277 $(diag(cov(C)))^{1/2}$. We define dissymmetric upper and lower bounds around the optimum for

278 the rigidity parameter $D = \frac{1}{c} \in \left[\frac{1}{c+dC}, \frac{1}{\max(c-dC, 10^{-4})} \right]$. To represent the uncertainty on the
 279 rigidity (dD) we use the fact that D is the inverse of the compliance and therefore:

$$dD = D^2 \cdot dC \quad (17)$$

280 **4. Determination of effective rigidity for a synthetic case**

281 Before running our optimization scheme on real cases, we evaluate its efficiency to recover a
 282 given rigidity distribution D^* (target rigidity) associated with a specific 2-D velocity field u^* .
 283 Surface strain across a locked fault zone can be interpreted either using the concept of a
 284 slipping fault zone beneath a locking depth (Savage and Burford, 1973) or by assuming a
 285 shear-rigidity variation perpendicular to the fault (Chéry, 2008). Differences and similarities
 286 between these models are discussed in this latter paper. According to the variable rigidity
 287 hypothesis, we define a target given by:

$$D^*(x) = 1 + \left(\frac{x}{d} \right)^2 \quad (18)$$

288 Where D^* is a non-dimensional rigidity, x is the distance to the fault and d is a characteristic
 289 dimension. Solving force balance within such a plate leads to the following fault-parallel
 290 velocity field:

$$u^* = \frac{s}{\pi} \arctan \left(\frac{x}{d} \right) \quad (19)$$

291 Therefore, such a velocity distribution is the solution of the spatially variable function of Eq.
 292 18 but can also be associated to a screw dislocation at depth (e.g., Savage and Burford, 1973).
 293 In the case of active fault systems, d is generally associated to a physical locking depth which
 294 can be estimated using geodesy and seismology. In the case of the San Andreas Fault system,
 295 values of d range from 6 to 22 km depending on the location along the fault and the method of
 296 determination (e.g. Smith-Konter et al., 2011).

297 We conduct two tests to verify the ability of the method to retrieve the rigidity distribution
 298 given by Eq. 18 for different GPS data sets. We also test different values of d (from 2 km to

299 17 km) in order to generate velocity fields commonly observed on the San Andreas Fault. The
300 specific case of fully-creeping faults ($d \sim 0$ km) is discussed in Appendix A, with application
301 to the SAF segment located North of Parkfield. We focus here on the consequences of
302 processing two different spatial distributions of GPS data: (1) evenly spatially distributed and
303 (2) concentrated near highly strained zones. This corresponds to on site situations (Fig. 3).
304 Both distributions are made of about 120 GPS velocities vectors.

305 Several experiments have been conducted to define an optimal mesh size. On the one hand,
306 the computational time is related to the mesh size. The finer is the grid, the longer will be the
307 optimization (about 60 times longer for a mesh 3.6 times finer). On the other hand, the grid
308 needs to be fine enough to capture the variations of the velocity field, notably close to high
309 velocity gradient areas such as the creep zones of the Parkfield segment. Eventually, a
310 spatially adaptive mesh should be implemented. We choose to work with a mean constant
311 spacing of 20 km. This configuration is generally a good compromise between the number of
312 available geodetic measurements, the number of parameters that need to be adjusted and the
313 size of the object we want to study.

314 For the first case, GPS measurements (black arrows on Fig. 3) are uniformly distributed over
315 the domain, with a constant spacing of 20 km. For the second distribution, we mimic a “real”
316 GPS network by producing a velocity field whose spatial density decreases with the distance
317 to the fault. In both cases, the domain is a 200-km square with a 20-km mesh size (394
318 elements). The dextral strike-slip fault (green line on Fig. 3) has a slip rate s of 30 mm/yr and
319 is locked at 10 km depth. The admissible values for the non-dimensional relative rigidity
320 range from 1 to 100 (see Appendices A and B for a discussion of such a choice).

321 We apply our optimization algorithm to invert the two velocity fields (Fig. 4 and 5). In the
322 case of the uniform dataset (Fig. 4 a-f), we first compare the synthetic velocities (red dots on
323 Fig. 4e) to the modelled ones (grey dots on Fig. 4e) along a profile (white dashed line on Fig.

324 4a) perpendicular to the fault (black dashed line on Fig. 4a-c). The dataset from the inversion
325 almost perfectly matches the characteristic shape of a 2-D arctangent velocity field given by
326 Eq. 19 (Fig. 4e). The misfit between predicted D and theoretical D^* (Fig. 4d) permits to
327 estimate the tendency in over or under estimating D in our inversions. Besides, the difference
328 between synthetic and modelled velocities, hereafter called residual velocities, is lower than
329 0.25 mm/yr over the whole domain (Fig. 4c).

330 Contrary to real cases where the true effective rigidity distribution is unknown, synthetic
331 cases allow for testing the efficiency of our inversion method to retrieve the quadratic rigidity
332 field given by Eq. 18. Fig 4a shows the rigidity distribution over the whole domain of
333 analysis, while Fig. 4b shows the uncertainty distribution map and Fig. 4f focuses along one
334 transect across the fault. We can notice that, as expected, the code predicts a low rigidity zone
335 (90% of the elements ranging between 1 and 3) along a 40 km-wide area centred on the fault.
336 Also, D increases rapidly with the distance to the fault to reach high values (>30) 60 km from
337 the fault. Associated with these rigidity values, we find uncertainties that are very small where
338 rigidity is small but quite high when the opposite occurs (Fig. 4b). This mainly comes from
339 the predominance of the (squared) rigidity term in Eq. 17. This expresses the fact that, in areas
340 that do not deform significantly, very large values of rigidity are admissible (up to infinity)
341 without modifying significantly the local velocity field. Since our search interval for rigidity
342 is bounded, our optimal solutions tend to underestimate the real rigidity in non-deforming
343 areas. This can be seen far from the fault in all the synthetic cases presented in this study (Fig.
344 4, 5, A.1 and A.2). Finally, we find that, within the uncertainties estimated by our method
345 (paragraph 3.4), our predicted rigidity distribution fits its theoretical value. This is clearly true
346 along the transect crossing the fault on Fig. 4f.

347 For a data set whose density decreases with distance to the fault (Fig. 5a-f), we observe the
348 same ability for the optimization algorithm to retrieve an arctangent-shaped velocity field

349 (Fig. 5f) and this despite sparse data away from the fault. In this synthetic case, some
350 elements of the grid contain more than one velocity, making the capture of very local velocity
351 gradients difficult if not impossible using one single rigidity parameter over each mesh
352 element. Therefore, residual velocities (Fig. 5c) are generally higher for case 2 than for case 1,
353 with 10% of residual vectors greater than 1 mm/yr (the 1σ uncertainty associated with the
354 data being 2 mm/yr) mainly located in the vicinity of the fault where each element of the grid
355 contains several GPS measurements. As a result, local gradients are more difficult to estimate
356 than for case 1 and this could explain the distribution of residual we observe in Fig. 5c.
357 Despite these moderate residuals, the mean residual velocity over the whole dataset is as low
358 as 0.85 mm/yr which is lower than the 1σ uncertainty of the data. This situation is typical of
359 real dataset with a high density of GPS installed in highly deformed areas.

360 Finally, as for the uniform case, we find that our inversion leads to a distribution of rigidity
361 that fits well its theoretical model within the predicted uncertainties (Fig. 5f). Indeed,
362 considering the 40-km band width around the fault, (Fig. 5a) shows that 66% of the elements
363 show low rigidities (between 1 and 3) while 29% present moderate ones (between 3 and 10).
364 As described above, in very few deforming areas, the optimal solution underestimates the real
365 rigidity but the uncertainty associated with these high values of rigidity tends to be quite high.
366 Moreover, the uncertainty values also depend on the local density of geodetic measurements.
367 Consequently, even when the optimization leads to fairly correct values of low-to-moderate
368 rigidity close to the fault, their uncertainties may be large (Fig. 5b) as one can see along the
369 transect between 20 and 100 km especially if the data distribution is random (Fig. 5f). Again,
370 we present the misfit between D and D^*

371 Overall, the satisfactory results of this experience lead us to keep this dimensioning of the
372 grid (triangles with about 20 km edges) for the real case application below.

373

5. EFFECTIVE RIGIDITY OF WESTERN USA

5.1 Tectonic context and GPS data

The tectonic of the Western United States mostly occurs in response to the relative motion between the Pacific plate and the North American plate. Two main zones accommodating the deformation are the San Andreas Fault system zone and the Basin and Range. In northern California, the relative motion between the Pacific plate and the Sierra Nevada reaches a differential rate of 30 mm/yr and results in large earthquakes. East of the Sierra Nevada, a significant part of the deformation (~10 mm/yr) occurs within the Basin and Range over a broad fault system. To the south, most of the strain is accommodated by the San Andreas Fault system while the southern Basin and Range is relatively inactive (Kreemer and Hammond, 2007). Although significant vertical deformation can occur during seismic events (Landers 1992, Northridge 1994 or Hector Mine 1999 earthquakes, red stars on Fig.6), vertical motion observed in the area are nearly 10 times smaller than the horizontal velocities during interseismic periods (Smith-Konter et al., 2014). Consequently, we chose to analyse only horizontal motion.

We focus our study on the southern part of the San Andreas Fault system (SAFS) where high-quality spatially dense GPS measurements are available. We use the CMM3 (Southern California Earthquake Center Crustal Motion Map Version 3.0, SCEC CMM3) velocity field as it was published by Kreemer and Hammond (2007). It is supposed to represent the interseismic motion that affects our region of interest. This means that all transient motions induced by the seismic events of Landers, Northridge and Hector Mine have been modelled and removed. These data are associated with relatively homogeneous uncertainties of 1.2 mm/yr in average.

A Lambert conformal conic projection is used to project the GPS velocity field on a Cartesian frame. To evaluate the effect of the choice of the domain, we analyse two overlapping areas

399 shown in Fig. 6. We aim at checking that effective rigidity values remain invariant regardless
 400 of the chosen borders. The first area of interest, hereafter named Zone 1, is limited by a red
 401 dashed line on Fig. 6 and is identical to the one used by Chéry et al., (2011). Then, a
 402 translation moves Zone 1 by 100 km towards the Northeast to obtain the second region called
 403 Zone 2 (blue dashed lines on Fig. 6). Both areas include the central San Andreas Fault system
 404 (SAFS) segment, the Eastern California Shear Zone (ECSZ), the south Sierra Nevada (SN) to
 405 the North, the Mojave Desert (MD) in the centre, the Salton Sea (SS) and the south Basin and
 406 Range (SBR) to the East. The western part of Zone 1 contains a part of the Pacific Plate along
 407 the Californian coast whereas Zone 2 is directly bounded by the San Andreas fault to the
 408 West.

409

410 **5.2 Model parametrization and regularization coefficients**

411 According to the synthetic experiments presented above, we choose a uniform grid spacing of
 412 20 km. This configuration leads to meshes of 2284 elements.

413 At first, we attempt to evaluate the Tikhonov parameter λ_2 . To do so, we analyse the *trade-off*
 414 between the normalized regularization member of the functional along the domain
 415 boundaries, $M(u_{BC}) = \frac{R_2(u_{BC})}{\max(R_2(u_{BC}))}$, and the residual data misfit $Res(p)$ at all geodetic
 416 measurements within the domain (Fig. 7a). Each point of the curve represents an optimization
 417 for a given value of the regularization parameter λ_2 . A decrease of M corresponds to an
 418 increase of the regularization of the velocity field along the domain boundary, meaning that
 419 high gradient changes of u_{BC} are smoothed. This would confer some degree of smoothness to
 420 the solution. On the contrary, a reduction of regularization enables a better fit to high velocity
 421 gradient changes along the domain boundary. These particularly occur at the transition
 422 between highly deforming fault zones and rigid far fields. Nevertheless, this may induce
 423 undesirable velocity gradient variations where the velocity field is smooth. Hence, in order to

424 find the appropriate balance between the regularity of the boundary conditions and velocity
425 residual, we compare observed and modelled velocity distributions along the boundary (Fig.
426 7b-c-d). When the damping parameter is small (Fig. 7b), we allow the regularization term of
427 the functional to be high. This in turn permits to better fit the observed velocities close to the
428 boundaries and consequently within the domain. Nevertheless, the boundary solution may
429 show in some places a degree of sharpness that is not supported by any data. Increasing the
430 damping parameter used in Fig. 7c increases the regularity of the boundary conditions while
431 still fitting properly the data along the border. We observe that this is done without
432 significantly altering the fit between modelled and observed velocities. Finally, increasing the
433 damping parameter, which means that extremely smooth boundary conditions become
434 admissible, leads to incompatibility between modelled and observed velocities along the
435 border (Fig. 7d). From this analysis, we set the regularization parameter λ_2 to 10^{-3} for which
436 the balance between the regularization of the boundary conditions and the fit to observed
437 velocities within the domain appears to be optimal.

438 **5.3 Results of the inversion**

439 Considering the model geometry and parametrization previously described, we perform the
440 inversion of the GPS velocities for the two selected zones (Zone 1 and Zone 2) of the Western
441 United States.

442 ***5.3.1 Estimated relative rigidity and corresponding uncertainty distributions***

443 The inversion of the interseismic velocities leads to the distribution of effective rigidity
444 illustrated by Fig. 8a-b. In the case of Zone 1 (Fig. 8a), the lowest values of D (1-1.5) are
445 centered on the Mojave Desert, whereas slightly higher rigidities (1.5-4) are observed along
446 the San Andreas Fault system and in the extreme South of the Eastern California Shear Zone.
447 However, lower values of rigidity (associated with higher deformation rates) are expected
448 along the San Andreas Fault system rather than in the Mojave Desert. We expect that this

449 artefact is likely due to an over-correction of the post-seismic motion of the seismic events of
450 1992 (Landers), 1994 (Northridge) and 1999 (Hector Mine) within the CMM3 velocity field
451 (Liu et al., 2015) . When the GPS data are processed to only keep the interseismic velocity,
452 the post-seismic answer of the earthquakes is estimated at its best. This artefact in our results
453 could help identify the residual post-seismic motion left in the data. As for the high rigidities
454 (>12), they are associated to the South Basin and Range and the South Sierra Nevada where
455 no significant deformation needs to be accommodated. As an extension of Zone 1, the
456 inversion in Zone 2 (Fig. 8b) produces similar rigidity distribution along the SAF and the
457 extreme South of the ECSZ (1.5-4), with, again a surprisingly low rigidity (<1.5) in the
458 Mojave Desert. However, one main difference can be underlined as a zone with rigidity
459 ranging from 6 to 12 is found in the eastern part of the South Basin and Range.

460 As described in paragraph 3.4, we determine the uncertainties associated with our rigidity
461 estimation which essentially result both from the local measurement density and the
462 uncertainties associated with the data themselves. For each mesh element, we estimate the
463 lower and upper admissible value for rigidity (Fig. 9a-b). First, along all the active fault
464 systems, identified rigidity values are quite low as the amplitude between the upper and lower
465 bounds are lower than 3. The reliability of our solution in deforming zones comes from the
466 local high density of measurements and from large amplitude of the deformation. Conversely,
467 when entering rigid zones, where only few measurements are available, the uncertainties
468 increase very much reaching values that typically range from 2.5 to above 16 by several
469 orders of magnitude. This is notably the case East of the ECSZ. Although the distribution of
470 rigidity shown in Fig. 8a suggests an optimal value of 6-12, uncertainties in this area (Fig. 9)
471 indicate that a much larger rigidity value (higher than 16 by several orders of magnitude) is
472 also valid. This can be noted in the inversion over the shifted domain (Fig. 8b).

5.3.2 Associated residual velocities

473
474 Alongside with the distribution of the rigidity, we evaluate the difference between GPS and
475 the modelled velocities to produce the residual map (Fig. 10a-b). The fit between observed
476 and modelled data is estimated using the normalized root mean square (*NRMS*) (McCaffrey,
477 2005),

$$NRMS = \left[0.5N^{-1} \left(\sum_{i=1}^N \left(\frac{r_i^e}{\sigma_i^e} \right)^2 + \left(\frac{r_i^n}{\sigma_i^n} \right)^2 \right) \right]^{1/2} \quad (20)$$

478 where *e* and *n* stand for the eastern and northern directions respectively, *r* is the residual
479 velocity, σ the data standard error and *N* the number of data. In addition to the *NRMS*, the
480 weighted root mean square (*WRMS*) gives a measure of the *a posteriori* weighted scatter in
481 the fits (McCaffrey, 2005),

$$WRMS = \left[\left(\sum_{i=1}^N \left(\frac{r_i^e}{\sigma_i^e} \right)^2 + \left(\frac{r_i^n}{\sigma_i^n} \right)^2 \right) / \left(\sum_{i=1}^N \left(\frac{1}{\sigma_i^e} \right)^2 + \left(\frac{1}{\sigma_i^n} \right)^2 \right) \right]^{1/2} \quad (21)$$

482 For Zone 1 (Fig. 10a), we get a *NRMS* of 1.26, with a *WRMS* of 1.10 mm/yr that can be
483 compared with the uncertainty of 1.20 mm/yr associated with the data. The highest residuals
484 (>4.5 mm/yr) occur on the southern segments of the SAF, while intermediate residuals (2.5-
485 4.5 mm/yr) are unevenly distributed between high and low data density zones.

486 A similar analysis for Zone 2 gives a *NRMS* of 1.25 (Fig. 10b) with a *WRMS* of 0.93 mm/yr.
487 The difference observed in the values of both zones can be explained by the data distribution.
488 Indeed, the second zone excludes some of the velocities that are poorly estimated by the
489 optimization (notably on the Pacific plate) and includes few vectors that are better recovered.

490

491 6. DISCUSSION

492 Based on the hypothesis that interseismic strain mostly reflects rheological contrasts across
493 the lithosphere, the solved inverse problem entirely depends on the quality of the CMM3

494 velocity field. Therefore, we first discuss the sensitivity of the model result with respect to the
495 data. Then, we discuss our results (strain rate and rigidity distributions) in the light of the ones
496 provided by previous studies on western US and California. We finally discuss the future use
497 of our method for tectonic and geodynamic purposes.

498 **6.1 Robustness of the inversion**

499 In this study, we use the entire dataset of the Southern California Crustal Motion Map Version
500 3.0, involving 615 vectors for Zone 1 and 530 vectors for Zone 2. In order to evaluate the
501 impact of data selection on rigidity distribution, we perform complementary inversions using
502 identical parametrization, but removing GPS vectors whose residual norms r are greater than
503 a given threshold value. These residuals can be due to three different factors:

- 504 1) **GPS uncertainty.** Data uncertainties range from 0.16 mm/yr to 3.71 mm/yr for the
505 horizontal components with a *RMS* value of 1.20 mm/yr. The maximum data
506 uncertainties are observed in the South of Mojave Desert, along the Los Angeles Bay
507 and for a few isolated points in the Sierra Nevada and ECSZ.
- 508 2) **Local motions.** Besides interseismic plate motions, some sites may be affected by
509 gravitational collapse, geothermal activity (e.g. Vasco et al., 2002) or the exploitation
510 of aquifer systems (e.g. Galloway et al., 1998; Hoffmann et al., 2001). Many different
511 processes can locally obscure the GPS interseismic velocity component, such as
512 unravelled postseismic motions.
- 513 3) **Modelling.** The optimization algorithm and the forward model can also be at the
514 origin of the residual velocities. Indeed, a poor estimation of the velocity along the
515 boundaries could be the reason why high residual velocities are observed at the
516 junction between the fault and the boundaries of the domain for both synthetic and real
517 data cases. Furthermore, our forward model includes several assumptions such as an
518 absence of body forces. Also, the data are assumed free of post-seismic effects which

519 can be inexact if all post-seismic effects due to the Landers, Northridge and Hector
520 Mine earthquakes, for instance, have not been fully removed.

521 We choose to withdraw from 0.3% ($r > 6$ mm/yr) up to 50% ($r > 1.3$ mm/yr) of the data in
522 order to analyse the stability of the solution of our inversion. The corresponding *NRMS*,
523 *WRMS* and the correlation of the rigidity distribution with respect to the one obtained by the
524 previously described inversion are gathered in **Error! Reference source not found.** We
525 choose experiment 1 as the reference solution to estimate the rigidity correlation. Removing
526 up to 10% of the GPS measurements exhibiting significant residuals in our initial inversion
527 (experiences 3 to 6 in Table 1) neither enhance the *NRMS* or the *WRMS*, nor significantly
528 modify the rigidity distribution. But considering only 50% of the data (experience 7 in Table
529 1) improves the *NRMS* to 0.67 and the *WRMS* to 0.54 mm/yr and leads to a rigidity
530 correlation of 0.831 with the main features preserved.

531 This approach echoes the strategy Meade and Hager (2005) developed to reduce the number
532 of stations and therefore to minimize the uncertainty magnitude. While based on different
533 quality criteria, they remove about 50% of the initial dataset (CMM3) to compute their
534 inversions. Our results illustrate that selecting the data with the lowest residuals does not
535 significantly influence the modelled rigidity (see correlation in Table 1). However, in areas
536 where data density is poor, a reduction of 50% can lead to a completely different
537 interpretation. Therefore, keeping the whole dataset seems preferable.

538 **6.2 Strain rate: comparison with other approaches**

539 Most of strain rate computations derived from GPS velocity measurements stand on a
540 continuous approximation of a model velocity field. A simple way to compute the strain rate
541 is to design a triangulation of the GPS points collection and then assume that the velocity field
542 inside each triangle evolves linearly. However, this method generates a non-smooth strain
543 map due to a linear interpolation of measured GPS velocities. This method can be adapted to

544 areas covered by sparse GPS networks (Masson et al., 2005) but generates erroneous strain
545 rates when applied to dense networks such as the ones installed in California. In this case, a
546 smooth approximation of the velocity field needs to be performed in order to avoid spurious
547 strain rate modeling. Consequently, a suitable method must also account for high strain
548 gradient occurring around fault zones. A large variety of mathematical approaches can be
549 used to deduce a strain rate map, often leading to relatively large differences (Feigl et al.,
550 1993; Mc Caffrey et al., 2005; Shen et al., 1996; Tape et al., 2009).

551 Our optimal solution of rigidity distribution can be used for the determination of strain rates
552 over the whole study area. But, we have shown above that our models systematically
553 underestimate rigidity in very few deforming areas, typically far from the active fault systems.
554 This bias is partly counterbalanced by the information provided by the upper bound of the
555 admissible rigidity values. These latter are very close to the optimal solution in deforming
556 zones, while they suggest that a purely rigid behavior may be considered when the
557 deformation is very small, even though a slight deformation remains admissible just
558 considering geodetic measurements. Therefore, using this “strongest” admissible solution is a
559 way to conform to geological considerations and block-model assumptions that state that, in
560 most cases, far from the faults, the blocks are rigid. So, we used the upper bound rigidity
561 distribution (Fig. 9b) for creating our strain rate map (Fig. 11a).

562 We compare in Fig. 11 our strain rate map (through the 2nd invariant of the strain tensor) with
563 the one obtained by a method originally proposed by Haines and Holt (1993) and later revised
564 in the framework of the strain map global project (Kreemer et al., 2014). Although both
565 methods depend on distinct assumptions, they produce similar intensities (> 64 nanostrain/yr)
566 located near faulted areas along the SAF and the ECSZ. This overall similarity is probably
567 due to the fact that both approaches are able to produce a low residual between the discrete
568 and the continuous velocity fields. Using our strongest admissible rigidity solution leads to

569 low strain estimates in weakly deforming areas that are similar to the ones obtained by the
570 global strain map project. This can be noticed in the Great Valley between the SAF and the
571 Sierra Nevada and along the Pacific coast.

572 A significant difference between the two strain rate maps can be found only on two limited
573 areas: offshore the Pacific coast and east of the ECSZ. Because these two areas display low
574 residuals (Fig. 10), we guess that our model is likely not able to locally estimate the strain rate
575 precisely. This could be due on the one hand, to an improper estimate of the boundary
576 conditions notably within the Pacific plate, and on the other hand, to a very low local data
577 density. Indeed, whereas Kreemer et al. (2014) only interpolate the strain rate dataset to best
578 fit the data, our solution aims at doing the same, but under the constraint of the stress
579 equilibrium equation (Eq. 1). As demonstrated by the synthetic benchmarks presented in
580 paragraph 3.4, evenly distributed data lead to a better estimation of the rigidity. Therefore, a
581 future use of our methodology could be to invert interpolated GPS velocities (such as the ones
582 provided by the Global Strain Rate Project) instead of the original GPS data to compute
583 effective rigidity distribution at a continental scale.

584 Lastly, we compare the spatial distribution of our dilatational strain rate solution with the one
585 obtained by Kreemer et al. (2014) (Fig. 12). We use the first invariant of the strain rate tensor
586 (mean of its trace) as a first-order approximation of the dilatational strain rate.

587 Neither the strain compatibility approach used by Kreemer et al. (2014) nor our study, take
588 vertical velocity measurements into account. Nevertheless, the plane stress formalism of our
589 modelling leads to the prediction of vertical strain rates, which is not the case in Kreemer et
590 al. (2014) analysis. Yet, recent analyses (e.g., Becker et al., 2015) suggest that the rate-change
591 of vertical loading of the lithosphere may play a dominant role in defining the distributions of
592 seismicity and therefore strain.

593 Despite the difference in their estimation, both spatial distributions of the dilatation strain rate
 594 from Kreemer et al. (2014) and us are very similar. They notably highlight the compressive
 595 context of the SAF system along the central bend. The only noticeable difference can be
 596 found along the fault system located north of Los Angeles where vertical motion is known to
 597 occur along active thrust faults (e.g. Northridge or Compton faults).

598 **6.3 Rigidity of the lithosphere and effective elastic thickness**

599 In the following, we study the relation between in-plane rigidity associated with geodetic
 600 strain (this work) and the flexural rigidity deduced from gravity and topographic data analysis
 601 (Audet and Bürgmann, 2011; Lowry and Pérez-Gussinyé, 2011; Tesauro et al., 2011). In the
 602 case of a thin curved elastic plate, the relation between the bending moment M and the
 603 flexural rigidity D_f is given by:

$$M = -D_f \frac{d^2w}{dx^2} = \frac{D_f}{R(x)} \quad (22)$$

604 where w is the vertical displacement of the plate and $R(x)$ its local curvature radius
 605 (e.g. Turcotte and Schubert, 2002). Using Eq. 2, a horizontal force per unit area applied to a
 606 vertical section of the lithosphere can be defined as:

$$F = D_g \left(\varepsilon_{ij} + \frac{\nu}{1 - 2\nu} \varepsilon_{kk} \delta_{ij} \right) \quad (23)$$

607 where D_g is the stiffness of the lithosphere to horizontal strain. D_g is equal to $2GT_g$ where G is
 608 the shear modulus (Pa) and T_g the plate thickness (m). Therefore, in-plane rigidity D_g is
 609 expressed in N while the flexural rigidity D_f is given in Nm, precluding a direct comparison
 610 between these two fields. In order to compare our relative rigidity map with the flexural
 611 rigidity deduced from gravity and topographic data analysis (Audet and Bürgmann, 2011;
 612 Lowry and Pérez-Gussinyé, 2011; Tesauro et al., 2011), we use the elastic thickness
 613 associated to these two formalisms.

614 The study of Lowry and Pérez-Gussinyé (2011) provides a map of the flexural elastic
615 thickness (T_e) for the entire western US. We assume that a linear relationship exists between
616 the in-plane plate rigidity and its corresponding thickness (Chéry, 2008 and present work).
617 Therefore, our map of T_g is directly proportional to the distribution of D shown in Fig. 8a.
618 Although such a linear relationship is valid only if elastic parameters do not vary with depth,
619 it provides a simple way to estimate the effective elastic thickness for our modelling. For the
620 purpose of comparison with Lowry and Pérez-Gussinyé (2011), we display their value of T_e
621 over Zone 1 (Fig. 13). Flexural and geodetic elastic thicknesses displayed in Fig. 13 show a
622 very limited degree of agreement. For example, the flexural thickness map predicts a thick
623 plate for most of the SAF, while a low geodetic elastic thickness is deduced using the
624 interseismic velocity field. The only area suggesting some resemblance corresponds to the
625 Basin and Range around the ECSZ and the SAF around the Salton Trough for which both
626 methods display low elastic thickness. In order to find some justifications about the large
627 discrepancies between T_e and T_g at least two lines of arguments could be investigated.
628 First, despite the formal similarity between flexural plate and shear plate theories (Chéry et
629 al., 2011), they may reflect two distinct lithospheric behaviours. For example, as stated by
630 Thatcher and Pollitz (2008), plate flexure is the result of a long term loading over millions of
631 years, implying that the strain rate in most of the lithosphere is close to zero. T_e is a measure
632 of stress that is supported dynamically over very long timescales by a lithosphere that is in a
633 state of frictional failure and viscoelastic flow, meaning the strain rate is virtually zero.
634 However, given the shorter timescale of geodetic observation and the clear evidence for
635 seismic release of significant elastic strain potential accumulated on century timescales, T_g
636 likely does predominantly reflects the elastic behavior of a thicker domain associated to
637 interseismic deformation. Another difference may come from the lithospheric loading.
638 Vertical loads modify distinct components of the strain tensor. Indeed, those induce flexure

639 and plate motions and therefore horizontal shear. Hence, distinct behaviours may emerge
640 from these kinds of load.

641 In the brittle part of the crust, background seismicity is likely to reflect the loading of
642 interseismic motion, therefore introducing an anelastic component into the analysed shear
643 motion. Beneath the crust and especially under a shear zone like the San Andreas Fault
644 system, the upper mantle presents a laterally variable and strong anisotropy (Hartog and
645 Schwartz, 2001). If such anisotropic behaviours occur at both crustal and mantle levels,
646 flexural and horizontal loading may activate two different rheological systems that could
647 result into significant differences in terms of effective elastic thickness.

648 A second way to investigate is to assume that flexural and geodetic thicknesses represent the
649 same mechanical concept. However, they could be differently revealed by the data because of
650 the formal differences between the two inverse problems. In the case of flexural thickness, the
651 determination of T_e is based on the correlation between topographic and gravimetric signal.
652 Among other factors, erosion can smooth or sharpen the topographic signal. Even if its
653 influence can be accounted for in modelling approaches (e.g. Forsyth, 1985), the impact of
654 erosion on the determination of T_e seems difficult to quantify due to large uncertainty
655 associated to past erosion. In addition, a geodynamical setting mostly involving shear motion
656 may not be adapted at all for a flexural plate analysis because such a motion is not likely to
657 produce neither topographic nor gravimetric signals. Last but not least, inverse theory of plate
658 flexure requires that flexural thickness cannot be determined for resolutions smaller than the
659 characteristic flexural wavelength (Watts, 2001). This also may explain why a sharp rigidity
660 variation across the SAF cannot be resolved by this method. Even if our methodology has
661 never been used prior to Chéry et al. (2001), the direct relation between shear strain and shear
662 rigidity is likely to produce high resolution estimate of geodetic thickness for zones where the
663 geodetic strain is well defined. Conversely, we acknowledge that our uncertainty analysis

664 predicts inaccurate rigidity determination in zones of low strain-rate like the Sierra Nevada.
665 Also, lithospheric loads like body forces and basal stress coming from mantle motion can
666 impact the strain-rate field and therefore altering the determination of the shear rigidity. The
667 identification of the importance of such effects must be tackled by future studies.

668 In order to better understand the discrepancy between flexural and shear analysis, a tractable
669 way would be to design a complete mechanical model of western US as it was done for
670 example by Pollitz et al. (2010). Such a model could be used to predict synthetic topographic,
671 gravimetric and deformation datasets obeying to momentum and constitutive equations. Then
672 these “data” could be inverted using the methodologies associated to flexural and shear
673 lithospheric deformation and compared to the rheological input of the forward model.

674

675 **7. CONCLUSION**

676 A global inversion strategy has been proposed for the identification of effective rigidity maps
677 using GPS velocity fields under minimum *a priori* assumptions. Taking advantage of the self-
678 adjoint nature of the governing equations, large dimensional problems coming from necessary
679 high resolution distribution of the rigidity have been considered. Compared to the previous
680 study carried out by Chéry et al. (2011), the results are now backed by uncertainty analysis
681 which suggests that the effective rigidity can only be accurately determined in moderate or
682 highly strained areas.

683 This is a high-resolution methodology which can be seen as a mechanical model to link shear
684 rigidity to interseismic strain with no prior knowledge of fault locations. The main limitation
685 of this approach relies to the plane stress hypothesis used in the forward model. Therefore, no
686 strain variation occurs with depth for a given horizontal location over the plate. This
687 behaviour is probably over simplified around active faults acting like screw dislocations as
688 proposed by Savage and Burford (1973). To complete what is presented here, the following
689 directions can be considered:

- 690 1) The 2D–effective rigidity model can be replaced by a 3D model of Western United
691 States including the effective elastic thickness as the main geophysical parameter.
692 Because this approach would include the full 3D strain rate tensor, it would provide a
693 more realistic approximation of the plate behaviour of the lithosphere especially
694 around faults.
- 695 2) The 2D approach can be used over wide areas, for instance at the continental plate
696 scale, after a splitting in patches. This would permit to determine large scale rigidity
697 maps in the framework of the global strain map project of (Kreemer et al., 2014).
- 698 3) The strong spatial correlation between low rigidity areas and active fault zones also
699 suggests that our methodology could be applied for deciphering active faults in
700 tectonically poorly known areas.

701

702 **ACKNOWLEDGEMENTS**

703 We thank Prof. Riad Hassani from Nice-Sophia Antipolis University for making available to
704 us his plane stress Finite Element code CAMEF. We also acknowledge Tony Lowry and an
705 anonymous reviewer for their constructive remarks and suggestions. The PhD of S. Furst is
706 supported by the Total Company and the LabEx NUMEV project (n° ANR-10-LABX-20)
707 funded by the «Investissements d’Avenir» French Government program, managed by the
708 French National Research Agency (ANR).

709

710 **BIBLIOGRAPHY**

- 711 Allaire, G., Jouve, F., Toader, A.M., 2004. Structural optimization using sensitivity analysis
712 and a level-set method. *J. Comput. Phys.* 194, 363–393. doi:10.1016/j.jcp.2003.09.032
- 713 Anderson, K., Segall, P., 2013. Bayesian inversion of data from effusive volcanic eruptions
714 using physics-based models: Application to Mount St. Helens 2004-2008. *J. Geophys.*
715 *Res. Solid Earth* 118, 2017–2037. doi:10.1002/jgrb.50169
- 716 Audet, P., Bürgmann, R., 2011. Dominant role of tectonic inheritance in supercontinent
717 cycles. *Nat. Geosci.* 4, 184–187. doi:10.1038/ngeo1080
- 718 Becker, T.W., Lowry, A.R., Faccenna, C., Schmandt, B., Borsa, A., Yu, C., 2015. Western
719 US intermountain seismicity caused by changes in upper mantle flow. *Nature* 524, 458–
720 461. doi:10.1038/nature14867
- 721 Bird, P., Kong, X., 1994. Computer simulations of California tectonics confirm very low
722 strength of major faults. *Geol. Soc. Am. Bull.* doi:10.1130/0016-
723 7606(1994)106<0159:CSOCTC>2.3.CO;2
- 724 Chéry, J., 2008. Geodetic strain across the San Andreas fault reflects elastic plate thickness
725 variations (rather than fault slip rate). *Earth Planet. Sci. Lett.* 269, 351–364.
726 doi:10.1016/j.epsl.2008.01.046
- 727 Chéry, J., Mohammadi, B., Peyret, M., Joulain, C., 2011. Plate rigidity inversion in southern
728 California using interseismic GPS velocity field. *Geophys. J. Int.* 187, 783–796.
729 doi:10.1111/j.1365-246X.2011.05192.x
- 730 Chéry, J., Zoback, M.D., Hassani, R., 2001. An integrated mechanical model of the San
731 Andreas Fault in central and northern California. *J. Geophys. Res.* 106, 22051.
732 doi:10.1029/2001JB000382
- 733 Dzurisin, D., 2003. A comprehensive approach to monitoring volcano deformation as a
734 window on the eruption cycle. *Rev. Geophys.* 41, 1001. doi:10.1029/2001RG000107

- 735 Feigl, K.L., Agnew, C., Dong, D., Hager, H., Herring, A., Jackson, D.D., Jordan, T.H., King,
736 W., Larson, M., Murray, M.H., Webb, F.H., 1993. Space Geodetic Measurement of
737 Crustal Deformation in Central and Southern California , 1984-1992. *J. Geophys. Res.*
738 98, 1984–1992.
- 739 Forsyth, W., 1985. Subsurface Loading and Estimates of the Flexural Rigidity of Continental
740 Lithosphere. *J. Geophys. Res.* 90, 12623–12632.
- 741 Galloway, D.L., Hudnut, K.W., Ingebritsen, S.E., Phillips, S.P., Peltzer, G., Rogez, F., Rosen,
742 P. a., 1998. Detection of aquifer system compaction and land subsidence using
743 interferometric synthetic aperture radar, Antelope Valley, Mojave Desert, California.
744 *Water Resour. Res.* 34, 2573. doi:10.1029/98WR01285
- 745 Haines, A.J., Holt, W.E., 1993. A Procedure for Obtaining the Complete Horizontal Motions
746 Within Zones Deformation of Strain Rate Data. *J. Geophys. Res.* 98, 12057–12082.
747 doi:10.1029/93jb00892
- 748 Hartog, R., Schwartz, S.Y., 2001. Depth-dependent mantle anisotropy below the San Andreas
749 fault system: Apparent splitting parameters and waveforms. *J. Geophys. Res.* 106, 4155.
750 doi:10.1029/2000JB900382
- 751 Hesse, M. a., Stadler, G., 2014. Joint inversion in coupled quasi-static poroelasticity. *J.*
752 *Geophys. Res. Solid Earth* 119, 1425–1445. doi:10.1002/2013JB010272
- 753 Hoffmann, J., Zebker, H.A., Galloway, D.L., Amelung, F., 2001. Seasonal subsidence and
754 rebound in Las Vegas Valley, Nevada, observed by synthetic aperture radar
755 interferometry. *Water Resour. Res.* 37, 1551–1566. doi:10.1029/2000WR900404
- 756 Ivorra, B., Mohammadi, B., Ramos, A.M., 2013. Design of code division multiple access
757 filters based on sampled fiber Bragg grating by using global optimization algorithms.
758 *Optim. Eng.* 1–19. doi:10.1007/s11081-013-9212-z
- 759 Kreemer, C., Hammond, W.C., 2007. Geodetic constraints on areal changes in the Pacific–

- 760 North America plate boundary zone: What controls Basin and Range extension? *Geology*
761 35, 943. doi:10.1130/G23868A.1
- 762 Kreemer, C., Klein, E., Shen, Z.-K., Wang, M., Estey, L., Wier, S., Boler, F., 2014. A
763 geodetic platemotion and Global Strain Rate Model. *Geochemistry, Geophys.*
764 *Geosystems* 130. doi:10.1002/2014GC005407.Received
- 765 Liu, S., Shen, Z.-K., Bürgmann, R., 2015. Recovery of secular deformation field of Mojave
766 shear zone in southern California from historical terrestrial and GPS measurements. *J.*
767 *Geophys. Res. Solid Earth* 120, 3965–3990.
- 768 Lowry, A.R., Pérez-Gussinyé, M., 2011. The role of crustal quartz in controlling Cordilleran
769 deformation. *Nature* 471, 353–357. doi:10.1038/nature09912
- 770 Lowry, A.R., Smith, R.B., 1994. Flexural rigidity of the Basin and Range-Colorado Plateau-
771 Rocky Mountain transition from coherence analysis of gravity and topography. *J.*
772 *Geophys. Res.* 99, 20123–20140.
- 773 Mao, A., Harrison, C.G.A., Dixon, T.H., 1999. Noise in GPS coordinate time series. *J.*
774 *Geophys. Res.* 104, 2797. doi:10.1029/1998JB900033
- 775 Masson, F., Chéry, J., Hatzfeld, D., Martinod, J., Vernant, P., Tavakoli, F., Ghafory-Ashtiani,
776 M., 2005. Seismic versus aseismic deformation in Iran inferred from earthquakes and
777 geodetic data. *Geophys. J. Int.* 160, 217–226. doi:10.1111/j.1365-246X.2004.02465.x
- 778 McCaffrey, R., 2005. Block kinematics of the Pacific-North America plate boundary in the
779 southwestern United States from inversion of GPS, seismological, and geologic data. *J.*
780 *Geophys. Res. Solid Earth* 110, 1–27. doi:10.1029/2004JB003307
- 781 Meade, B.J., Hager, B.H., 2005. Block models of crustal motion in southern California
782 constrained by GPS measurements. *J. Geophys. Res. B Solid Earth* 110, 1–19.
783 doi:10.1029/2004JB003209
- 784 Mohammadi, B., Pironneau, O., 2009. *Applied Shape Optimization for fluids*, 2nd Editio. ed.

- 785 Oxford University Press, Oxford.
- 786 Mohammadi, B., Pironneau, O., 2004. Shape Optimization in Fluid Mechanics. *Annu. Rev.*
787 *Fluid Mech.* 36, 255–279. doi:10.1146/annurev.fluid.36.050802.121926
- 788 Montelli, R., Nolet, G., Masters, G., Dahlen, F.A., Hung, S.-H., 2004. Global *P* and *PP*
789 traveltime tomography: rays versus waves. *Geophys. J. Int.* 158, 637–654.
790 doi:10.1111/j.1365-246X.2004.02346.x
- 791 Mossop, A., Segall, P., 1999. Volume strain within The Geysers geothermal field. *J. Geophys.*
792 *Res.* 104, 29113–29131. doi:10.1029/1999JB900284
- 793 Pérez-Gussinyé, M., Swain, C.J., Kirby, J.F., Lowry, A.R., 2009. Spatial variations of the
794 effective elastic thickness, T_e , using multitaper spectral estimation and wavelet methods:
795 Examples from synthetic data and application to South America. *Geochemistry,*
796 *Geophys. Geosystems* 10. doi:10.1029/2008GC002229
- 797 Plessix, R.E., 2006. A review of the adjoint-state method for computing the gradient of a
798 functional with geophysical applications. *Geophys. J. Int.* 167, 495–503.
799 doi:10.1111/j.1365-246X.2006.02978.x
- 800 Pollitz, F.F., McCrory, P., Wilson, D., Svarc, J., Puskas, C., Smith, R.B., 2010. Viscoelastic-
801 cycle model of interseismic deformation in the northwestern United States. *Geophys. J.*
802 *Int.* 181, 665–696. doi:10.1111/j.1365-246X.2010.04546.x
- 803 Rosen, P., Werner, C., Fieldind, E., Hensley, S., Buckley, S., Vincent, P., 1998. Aseismic
804 creep along the San Andreas Fault northwest of Parkfield, Ca measured by radar
805 interferometry. *Geophys. Res. Lett.* 25, 825–828. doi:10.1029/JB078i005p00832
- 806 Savage, J.C., Burford, R.O., 1973. Geodetic determination of relative plate motion in central
807 California. *J. Geophys. Res.* 78, 832. doi:10.1029/JB078i005p00832
- 808 Sella, G.F., Dixon, T.H., Mao, A., 2002. REVEL: A model for Recent plate velocities from
809 space geodesy. *J. Geophys. Res.* 107, 2081. doi:10.1029/2000JB000033

- 810 Shen, Z.K., Jackson, D.D., Ge, B.X., Bob, X.G., 1996. Crustal deformation across and beyond
811 the Los Angeles basin from geodetic measurements. *J. Geophys. Res.* 101, 27927–
812 27957. doi:10.1029/96JB02544
- 813 Smith-Konter, B.R., Sandwell, D.T., Shearer, P., 2011. Locking depths estimated from
814 geodesy and seismology along the San Andreas Fault System: Implications for seismic
815 moment release. *J. Geophys. Res.* 116, B06401. doi:10.1029/2010JB008117
- 816 Smith-Konter, B.R., Thornton, G.M., Sandwell, D.T., 2014. Vertical crustal displacement due
817 to interseismic deformation along San Andreas fault: Constraints from tide gauges.
818 *Geophys. Res. Lett.* 41, 3793–3801. doi:10.1002/2014GL060091
- 819 Tanaka, S., Obayashi, M., Suetsugu, D., Shiobara, H., Sugioka, H., Yoshimitsu, J., Kanazawa,
820 T., Fukao, Y., Barruol, G., 2009. P-wave tomography of the mantle beneath the South
821 Pacific Superswell revealed by joint ocean floor and islands broadband seismic
822 experiments. *Phys. Earth Planet. Inter.* 172, 268–277. doi:10.1016/j.pepi.2008.10.016
- 823 Tape, C., Liu, Q., Maggi, A., Tromp, J., 2009. Adjoint tomography of the southern California
824 crust. *Science* 325, 988–992. doi:10.1126/science.1175298
- 825 Tarantola, A., 2004. *Inverse Problem Theory and Methods for Model Parameter Estimation*,
826 Book. doi:10.1137/1.9780898717921
- 827 Tesauro, M., Burov, E.B., Kaban, M.K., Cloetingh, S.A.P.L., 2011. Ductile crustal flow in
828 Europe's lithosphere. *Earth Planet. Sci. Lett.* 312, 254–265.
829 doi:10.1016/j.epsl.2011.09.055
- 830 Thatcher, W., Pollitz, F.F., 2008. Temporal evolution of continental lithospheric strength in
831 actively deforming regions. *GSA Today* 18, 4–11. doi:10.1130/GSAT01804-5A.1
- 832 Tikhonov, A.N., 1943. On the stability of inverse problems. *Dokl. Akad. Nauk Sssr* 39, 195–
833 198.
- 834 Turcotte, D.L., Schubert, G., 2002. *Geodynamics*. Cambridge University Press.

- 835 Vasco, D., Wicks, C., Karasaki, K., 2002. Geodetic Imaging: High Resolution Reservoir
836 Monitoring Using Satellite Interferometry. *Geophys. J. Int.* in press, 555–571.
- 837 Vassilvitskii, S., Yannakakis, M., 2005. Efficiently computing succinct trade-off curves.
838 *Theor. Comput. Sci.* 348, 334–356. doi:10.1016/j.tcs.2005.09.022
- 839 Vernant, P., 2015. What can we learn from 20years of interseismic GPS measurements across
840 strike-slip faults? *Tectonophysics* 644–645, 22–39. doi:10.1016/j.tecto.2015.01.013
- 841 Watts, A.B., 2001. *Isostasy and flexure of the Lithosphere*. Cambridge University Press,
842 Cambridge.
- 843 Zaroli, C., Sambridge, M., Lévêque, J.J., Debayle, E., Nolet, G., 2013. An objective rationale
844 for the choice of regularisation parameter with application to global multiple-frequency
845 S-wave tomography. *Solid Earth* 4, 357–371. doi:10.5194/se-4-357-2013
- 846
- 847
- 848

849 **Appendix A) Application to shallow creeping faults**

850 In this appendix, we briefly discuss the way our approach deals with very high strain rates and
851 what this implies in term of prior search interval for the relative shear-rigidity values.

852 Three terms contribute to the spatial regularization (smoothing) of the modelled distribution
853 of relative rigidity and, consequently, the modelled velocity field. The first one simply comes
854 from mesh size and, therefore, from the spatial resolution of our model. Then, a Tikhonov
855 regularization term can be activated in the cost function (Eq. 5). Finally, a spatial smoothing
856 process is performed on the gradient of the functional (Fig. 2).

857 All these components of our approach are likely to limit the range of strain rates that can be
858 properly modelled. In particular, active faults exhibiting very shallow creep are supposed to
859 lead to local under-estimation of rigidity gradients.

860 In practice, the mesh size is a few kilometres (20 km in the case of this study over South
861 California), the Tikhonov regularization term is not active, and the smoothing process over
862 the gradient of the functional can have a very limited spatial extent. Despite the limitations of
863 the effects of these regularization components, we see that the whole range of the expected
864 strain rates (about 4 orders of magnitude) can hardly be captured by our approach.
865 Nevertheless, we demonstrate, hereafter, that (1) if the spatial sampling is high, then using a
866 4-order of magnitude search interval allows for a good fit to sharp velocity changes. (2) Using
867 a 2-order of magnitude search interval is sufficient in most cases, small but significant local
868 residues being present only in the case of extremely shallow creeping behaviour.

869 First, we run our inversion on synthetic cases that are similar to those presented in section 3,
870 but for which the locking depth is much shallower: 2 km (Fig. A.1) and 0 km (Fig. A.2). For
871 these experiments, the mesh size is set to 3km.

872 In the case of a 2-km locking depth, we find that exploring a 2-order of magnitude interval for
873 rigidity is sufficient to perfectly model the velocity field (Fig. A.1). The only significant

874 difference between the modelled and the theoretical values of the relative rigidity appears on
875 non-significantly deforming zones at distances higher than about 20 km from the fault.
876 Indeed, in these areas, we know that changing the relative rigidity by several orders of
877 magnitude has very small influence on the velocity prediction. So, again, we show that our
878 approach underestimates rigidity far from the active faults. Exploring a 4-order of magnitude
879 rigidity interval does not improve the fit to ground velocities. It only pushes a little bit away
880 the limit where the real rigidity is underestimated.

881 If we consider, now, the extreme case of a fault experiencing creep up to the ground surface,
882 then the strain rate across the fault is infinite. A similar analysis to the preceding case shows
883 that significant residues remain close to the fault (Fig. A.2). Yet, their amplitudes are very
884 small (no more than 2 mm/yr) except exactly on the fault itself. In such an extreme case,
885 indeed, extending the search interval of rigidity from 2- to 4-order of magnitude allows for the
886 proper modelling of the velocity field everywhere. Nevertheless, this better fit has been
887 obtained at the cost of the regularity of the rigidity distribution which is slightly altered in
888 non-deforming zones (upper and lower central areas).

889 Let's move now to the case of the SAF fault segment that is located north of Parkfield. This
890 segment is known to be experiencing very shallow creep (e.g. Rosen et al., 1998). We use a
891 10-km mesh size and run inversions varying the range of the admissible rigidity values and
892 the smoothing factors for the gradient of the cost function. All lead to the same solution that is
893 presented on Fig. A.3. Using a 4-order of magnitude search interval does not provide
894 additional information that would not have been captured by a 2-order of magnitude search
895 interval. This may be due to the 10-km resolution of our mesh, as well as the relatively low
896 density of GPS measurements in the CMM3 database, notably with respect to other high-
897 resolution measurements like InSAR.

898 In order to illustrate the efficiency of our modelling, we compare the modelled velocity field
899 with the CMM3 measurements along two profiles across the SAF system, one (A-B) just
900 south of the city of San Juan Bautista (Fig. A.3b), and the other (C-D) close to the city of
901 Parkfield (Fig. A.3c). It can be noticed that no significant pattern of the deformation, as
902 gathered by the CMM3 database, is missed by our modelling. Moreover, this good fit has
903 been obtained with a limited range for the admissible rigidity values, which, in turn,
904 guarantees some degree of regularity of the rigidity distribution, even on very few deforming
905 areas.

906

907 **Appendix B) Processing the SAF zone using a 4-orders of magnitude range for** 908 **admissible rigidity**

909 In the main body of this paper, we determine the relative rigidity distribution (both for
910 synthetic and real cases) from the exploration of a 2-orders of magnitude range of rigidity
911 values. Appendix A shows that, unless we need to deal with sharp velocity gradients that are
912 typically found on very shallow creeping fault segments, this rigidity range is sufficient to
913 properly fit the interseismic velocity field within their uncertainties. In this appendix, we
914 show that using a wider range of admissible rigidity value (4 orders of magnitude instead of
915 2) in the inversion process applied to Southern California leads to a very similar solution.

916 As noticed in Appendix A, the inversion becomes now longer and less steady. Nevertheless, it
917 converges to a solution which differs only in places where ground deformation is very small.

918 Indeed, setting the lowest relative rigidity value to 1, then most of the significantly deforming
919 areas exhibit relative rigidity values that are below 20 (Fig. B.1a). Only quasi non-deforming
920 areas require relative rigidity values on the order of 100 or above. But we know that, in very
921 weakly deforming zones, large changes of high rigidity values only lead to small changes in
922 strain prediction. Fig. B.1b shows that, as expected, using a wider search domain leads to a

923 similar solution where ground deformation is significant, and to a larger ratio between rigidity
924 in non-deforming zones relatively to deforming areas. However, both solutions (using a 2-fold
925 or 4-fold range of magnitude) fit the data globally in the same way. This confirms the fact that
926 a very large range of rigidity is admissible far from the active fault systems. This statement is
927 illustrated again by the lower and upper bound solutions (Fig. B.1b-c). The rigidity
928 distribution is well constrained in significantly deforming zones, lower and upper bounds
929 being close to the optimal solution, but badly constrained elsewhere. Typically, any value of
930 rigidity higher than 10 is an admissible solution for rigid areas.

931 In conclusion, we see that almost all the significant ground deformation is captured using a 2-
932 orders of magnitude range for relative rigidity. Increasing this range allows either a better
933 modelling of ground deformation induced by shallow surface creeping segments, or the
934 assignment of higher rigidity values in non-deforming zones. But, in this latter case, the fit to
935 the velocity field is very little improved and we know that the uncertainties associated with
936 these rigidity values remain very high.

Table 1[Click here to download Table: Table_1.docx](#)

| Experiment | Zone | Grid Size | Number of GPS vectors | <i>NRMS</i> of the residual velocities | <i>WRMS</i> (mm/yr) | Rigidity Correlation |
|-------------------|-------------|------------------|------------------------------|-----------------------------------------------|----------------------------|-----------------------------|
| 1 | 1 | 20 | 615 | 1.26 | 1.10 | 1 |
| 2 | 2 | 20 | 530 | 1.25 | 0.93 | 0.831 |
| 3 | 1 | 20 | 613 (99.7%) | 1.25 | 1.08 | 0.995 |
| 4 | 1 | 20 | 600 (97.5%) | 1.21 | 1.04 | 0.986 |
| 5 | 1 | 20 | 583 (94.7%) | 1.16 | 1.00 | 0.987 |
| 6 | 1 | 20 | 553 (90%) | 1.10 | 0.93 | 0.958 |
| 7 | 1 | 20 | 307 (50%) | 0.67 | 0.54 | 0.831 |

Table 1. List of the experiments, the *NRMS/WRMS* values of the residual velocities and the correlation of the rigidity distribution relatively to experiment 1.

Figure 1

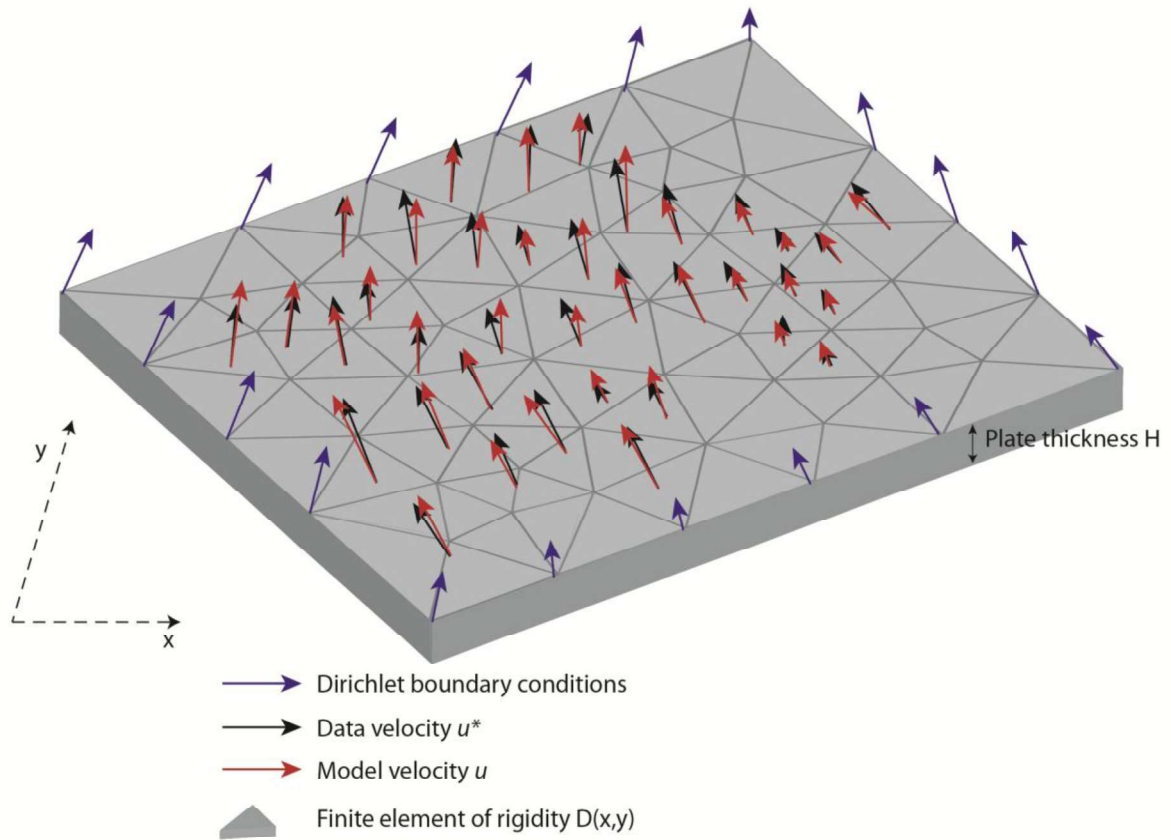


Fig. 1. Schematic representation of the optimization problem: the domain Ω is meshed with elements of constant rigidity $D(x, y)$ and submitted to Dirichlet boundary conditions along the boundary $\partial\Omega$. The black arrows symbolise the geodetic measurements u^* within the domain, the blue ones the Dirichlet conditions which are part of the optimization variables and the red ones are the solution of the model.

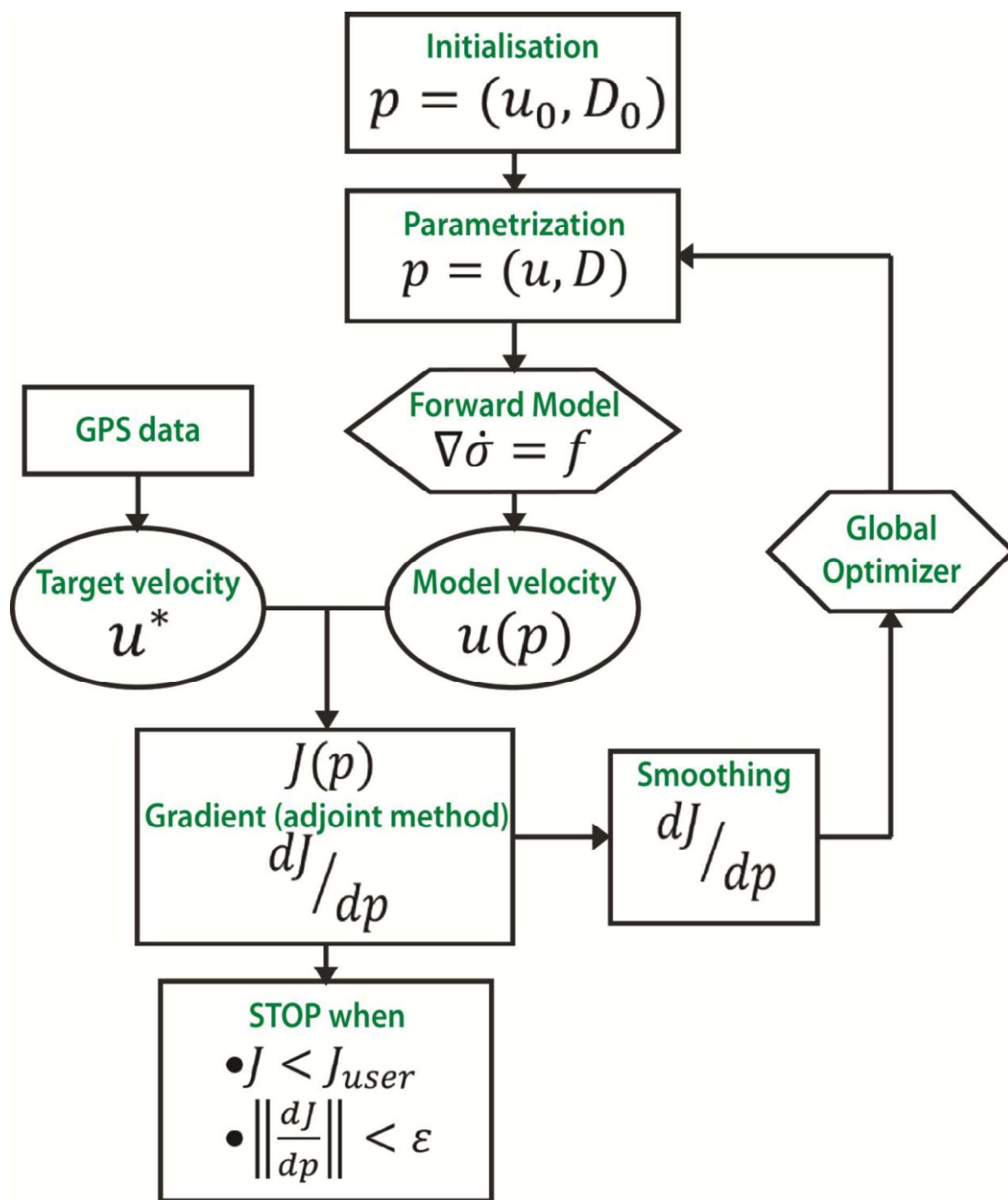


Fig. 2. Sketch of optimization algorithm applied to plate rigidity inversion. For each iteration we optimize both the rigidity within the domain and the velocity along the boundaries.

Figure 3

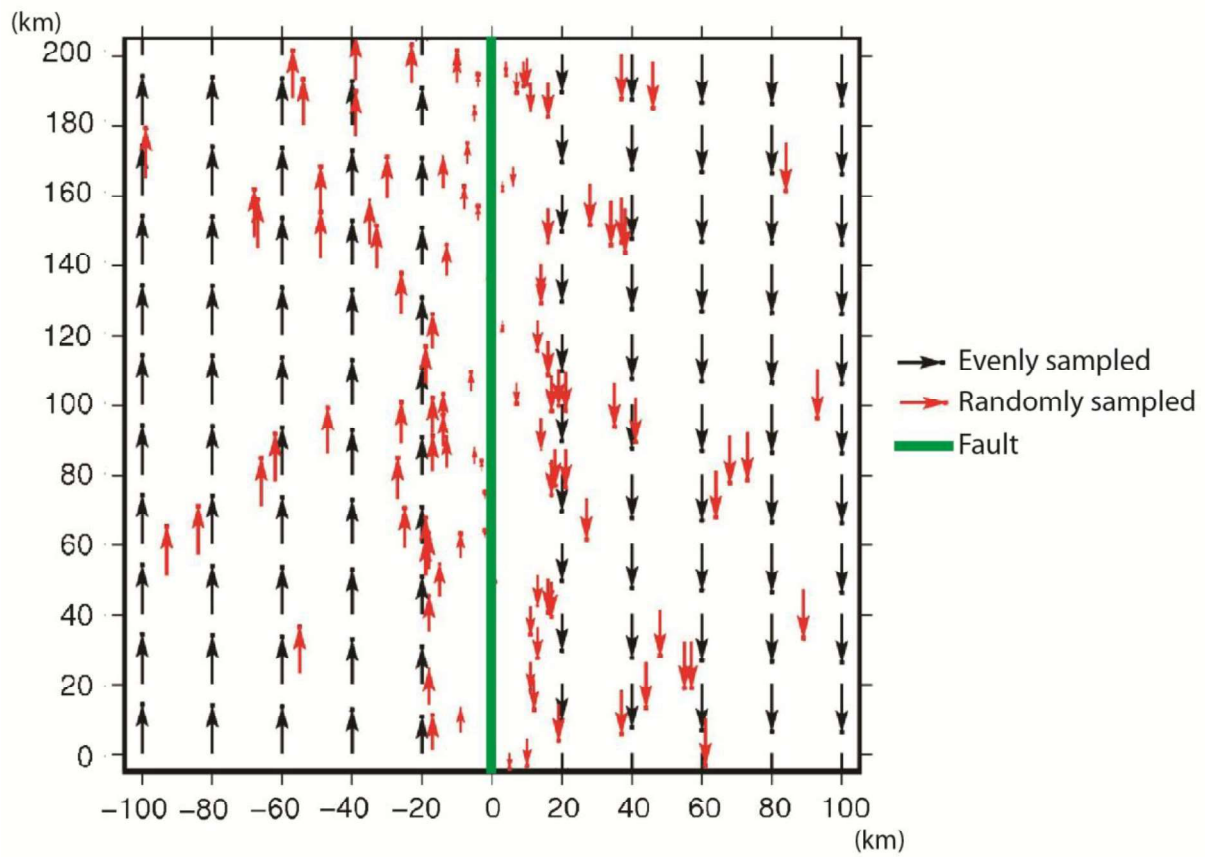


Fig. 3. Distribution of the synthetic velocities considering an evenly sampled domain (black arrows) and a randomly sampled domain whose density decreases with the distance to the fault (red arrows). The fault (green line) is a dextral strike slip fault locked during the interseismic motion.

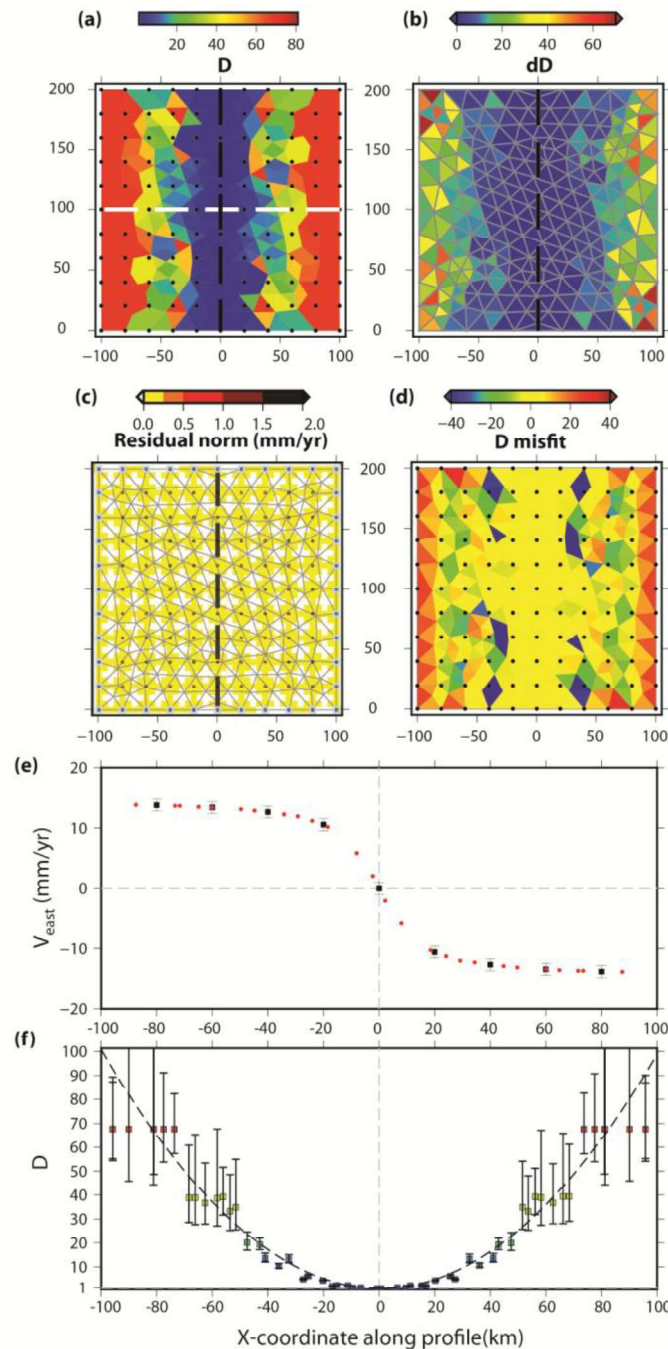


Fig. 4. Results of the inversion for the synthetic case with a geodetic spatial sampling (black dots on (a), (c) and (d)) whose density is constant whatever the distance to the fault (black line at coordinate 0 along the Y-axis). (a) rigidity distribution determined by the optimization; (b) associated uncertainty; (c) norm of residual velocities; (d) misfit between predicted D and theoretical D^* ; (e) velocity measurements (black squares with uncertainty bars) and velocities predicted by our model (red circles) along the profile shown in white dotted line on (a); (f) rigidity values and their associated uncertainties along the same profile. The plotted values are estimated at the barycentre of the elements of the mesh in a 30-km wide bandwidth centred on the profile. The colour code is the same as in (a).

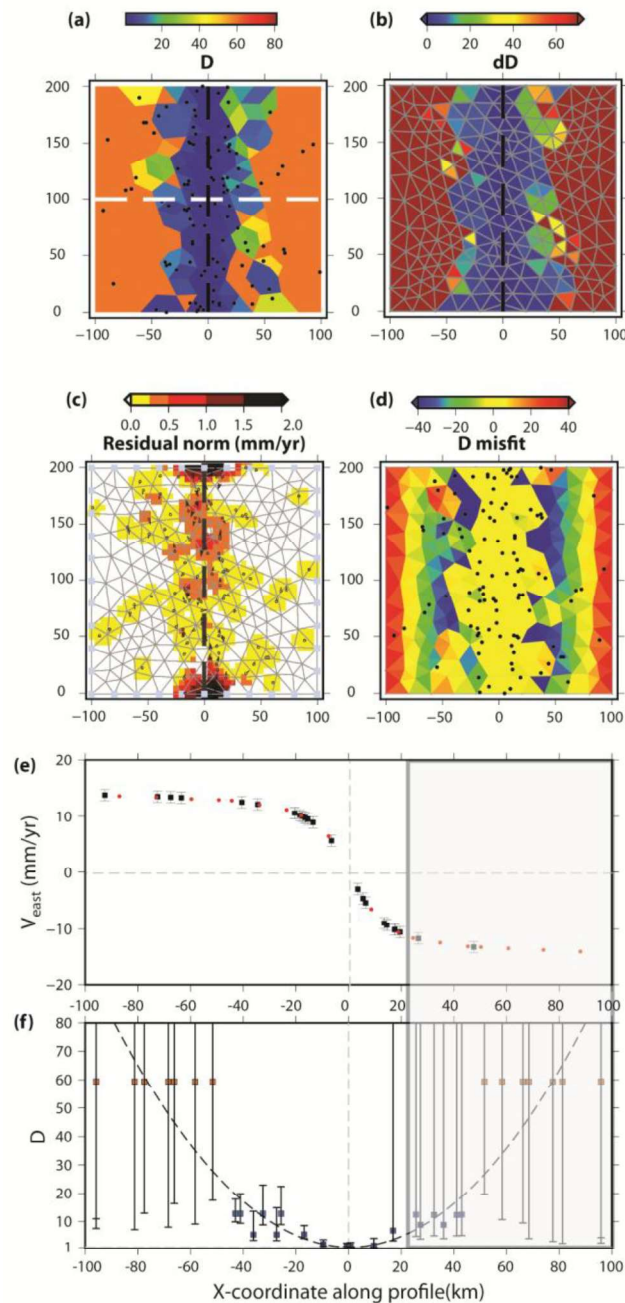


Fig. 5. Results of the inversion for the synthetic case that mimics a real geodetic spatial sampling (black dots on (a) (c) and (d)) whose density decreases with the distance to the fault (black line at coordinate 0 along the Y-axis). (a) rigidity distribution from the optimization; (b) associated uncertainty; (c) norm of residual velocities; (d) misfit between predicted D and theoretical D^* ; (e) velocity measurements (black squares with uncertainty bars) and velocities predicted by our model (red circles) along the South to North profile shown in white dotted line on (a); (f) rigidity values and their associated uncertainties along the same profile. The opaque rectangle over the northern termination of rigidity and velocity profile (e) and (f) highlights a zone where the density of measurements is low, leading to high rigidity uncertainties.

Figure 6

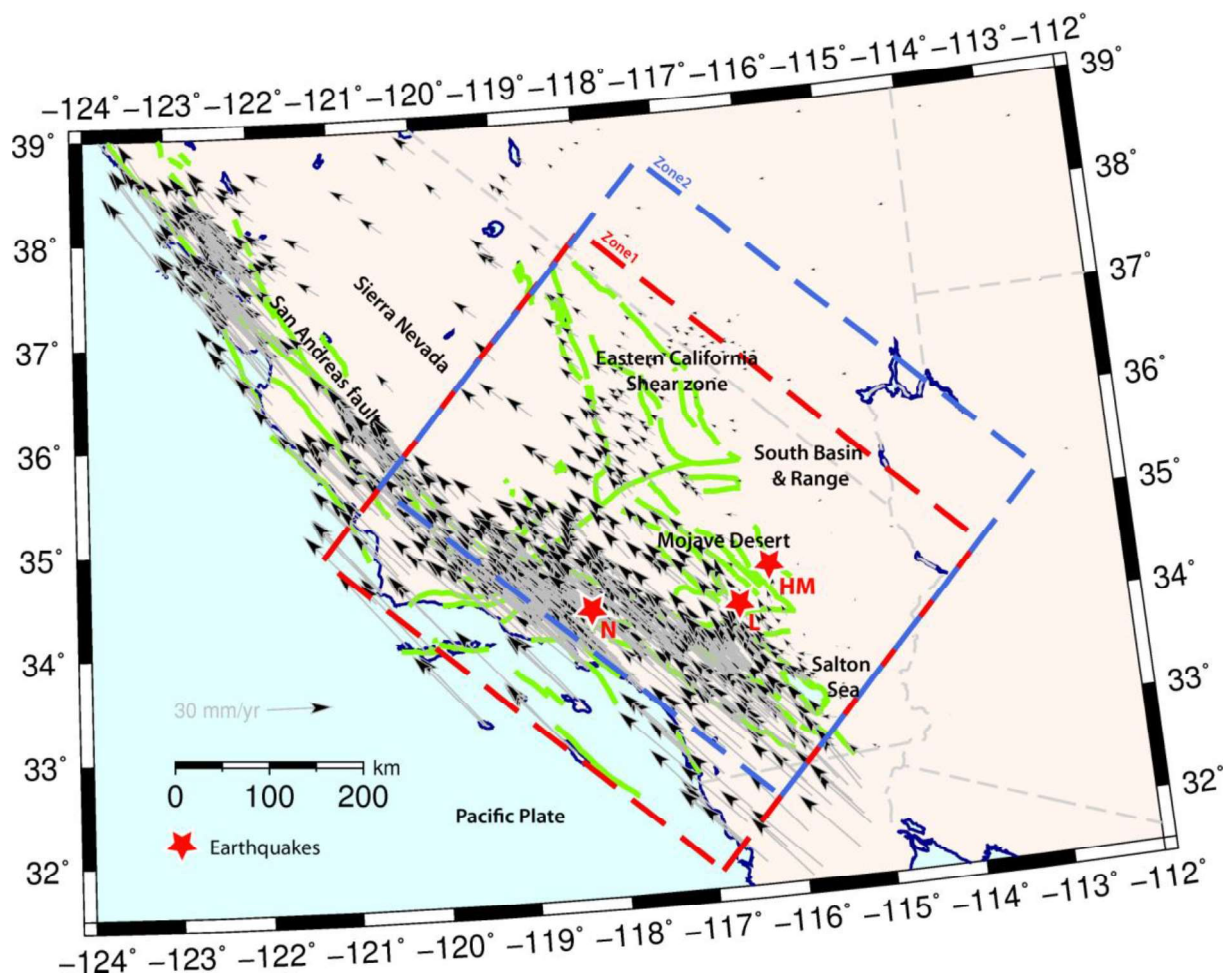


Fig. 6. Spatial distribution of the geodetic measurements on the SAF system used for the inversion. The black arrows show the velocity field in the North American reference frame. Our main domain of analysis is shown in the red rectangle (Zone 1 – 615 GPS velocities) while the blue one (Zone 2 – 530 GPS velocities) represents a translation of the area of interest. The red stars indicate the location of Landers (L), Northridge (N) and Hector Mine (HM) earthquakes.

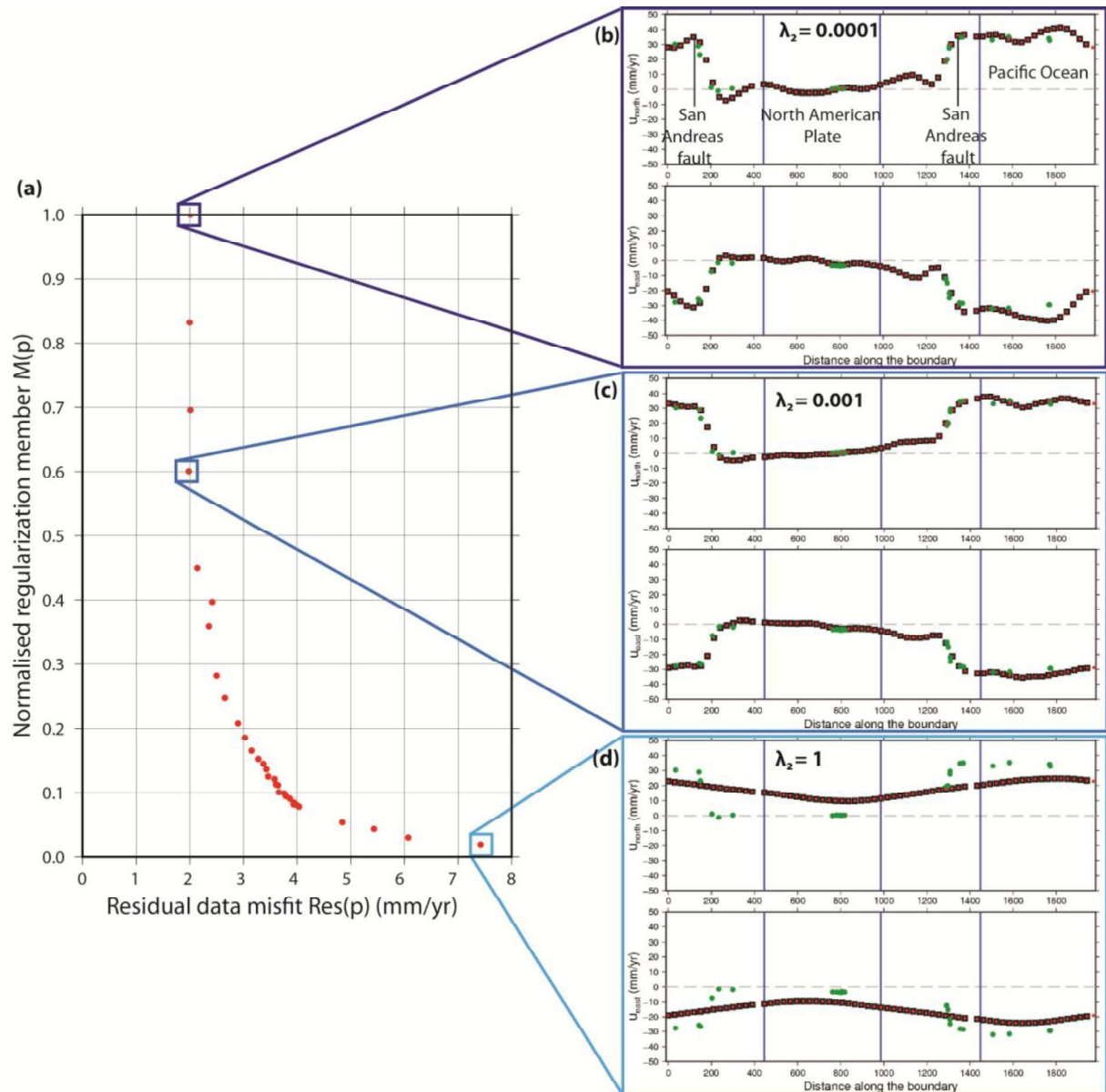


Fig. 7 Pareto curve for different regularization parameters used in the optimization algorithm applied to the southern California. (a) Plot of the normalized velocity variations norm as a function of the residual data misfit as damping λ_2 varies. (b), (c) and (d) represent the velocities observed within a 10-km distance of the domain boundary (green) and calculated on the boundaries (red) for different damping parameter λ_2 .

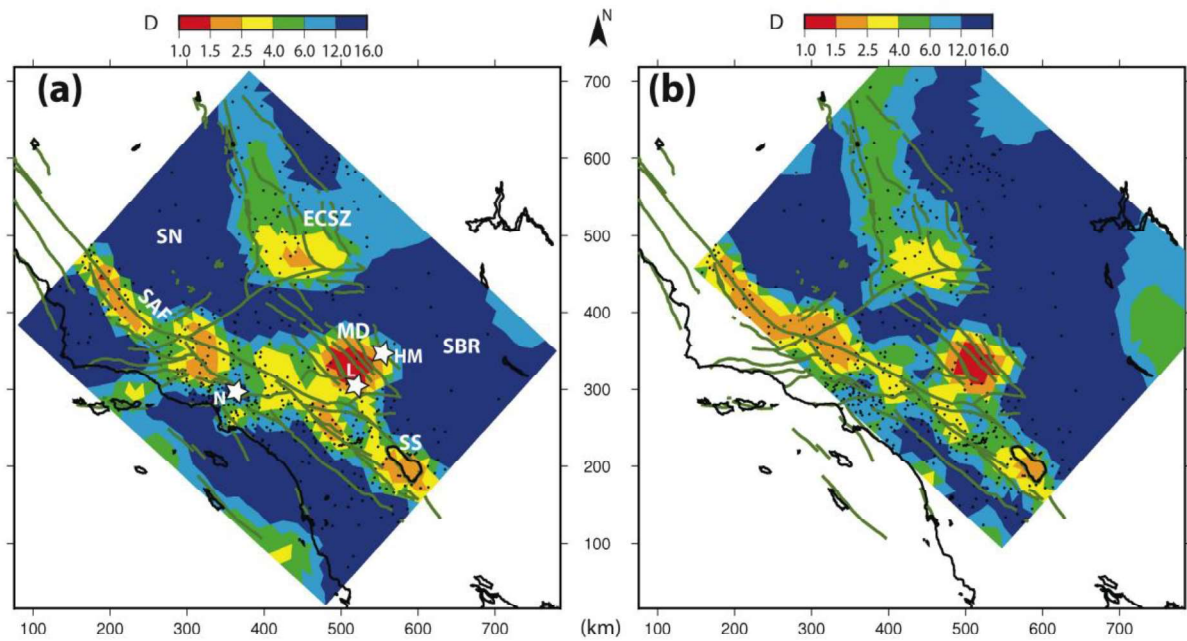


Fig. 8. Distributions of the relative rigidity D represented for Zone 1 (a) and for Zone 2 (b). According to Eq. 23, the elastic thickness T_g is proportional to D . The GPS data are represented by black dots, the faults by green lines and the Landers (L), Northridge (N) and Hector Mines (HM) earthquakes by white stars. SAF, SN, ECSZ, SBR, MD and SS stand for San Andreas Fault, Sierra Nevada, Eastern California Shear Zone, South Basin and Range, Mojave Desert and Salton Sea respectively.

Figure 9

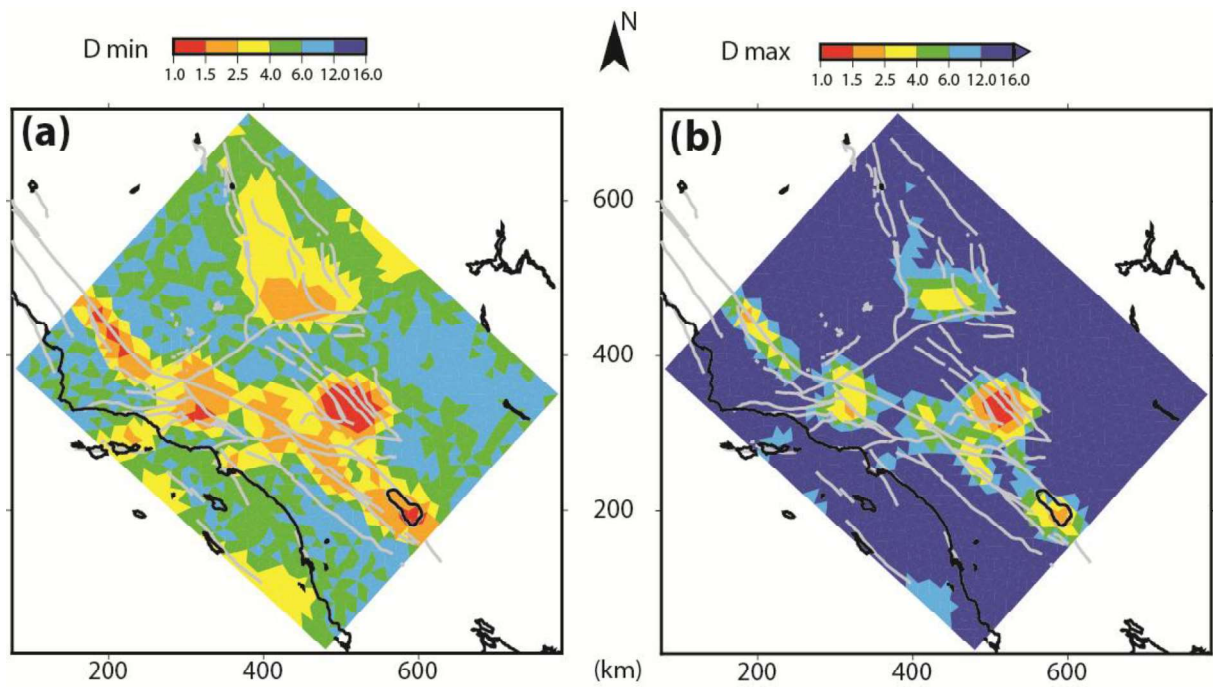


Fig. 9: (a) Lower and (b) upper bounds for the rigidity values around the optimal distribution displayed on Fig. 8a for Zone 1. In very few (or non-) deforming areas, D_{max} reach values that are several orders of magnitude higher than the optimal solution.

Figure 10

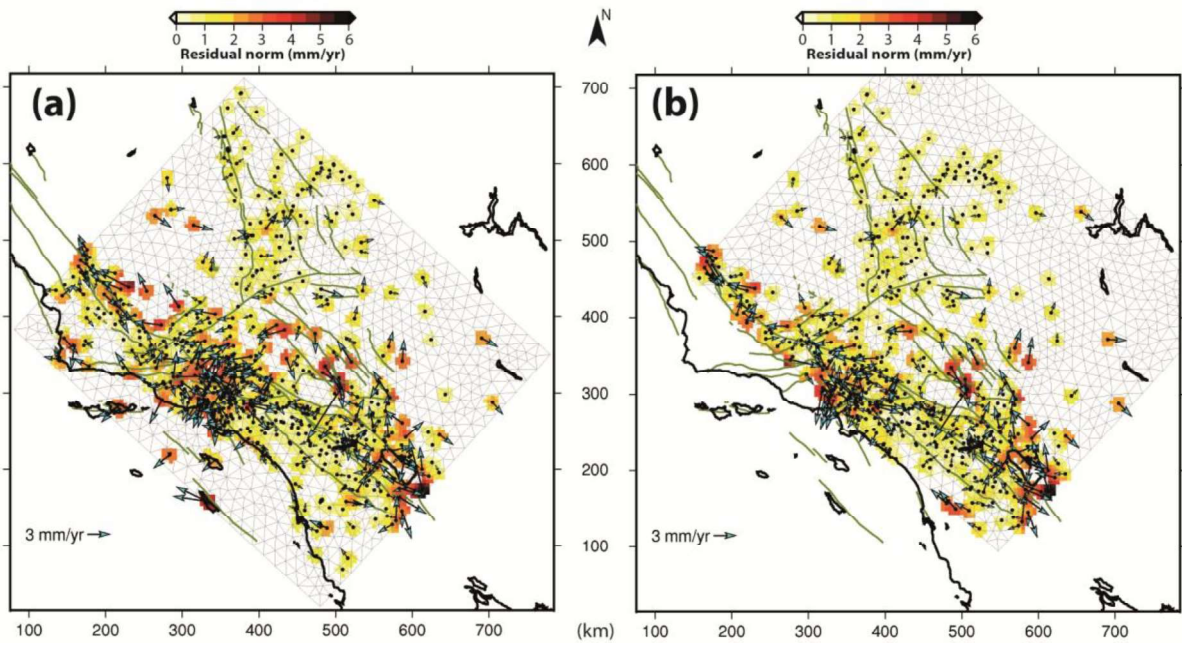


Fig. 10. Norm of residual velocities between GPS and modelled velocities associated with the rigidity distribution determined for a) Zone 1 ($NRMS=1.26$) and b) Zone 2 ($NRMS =1.25$).

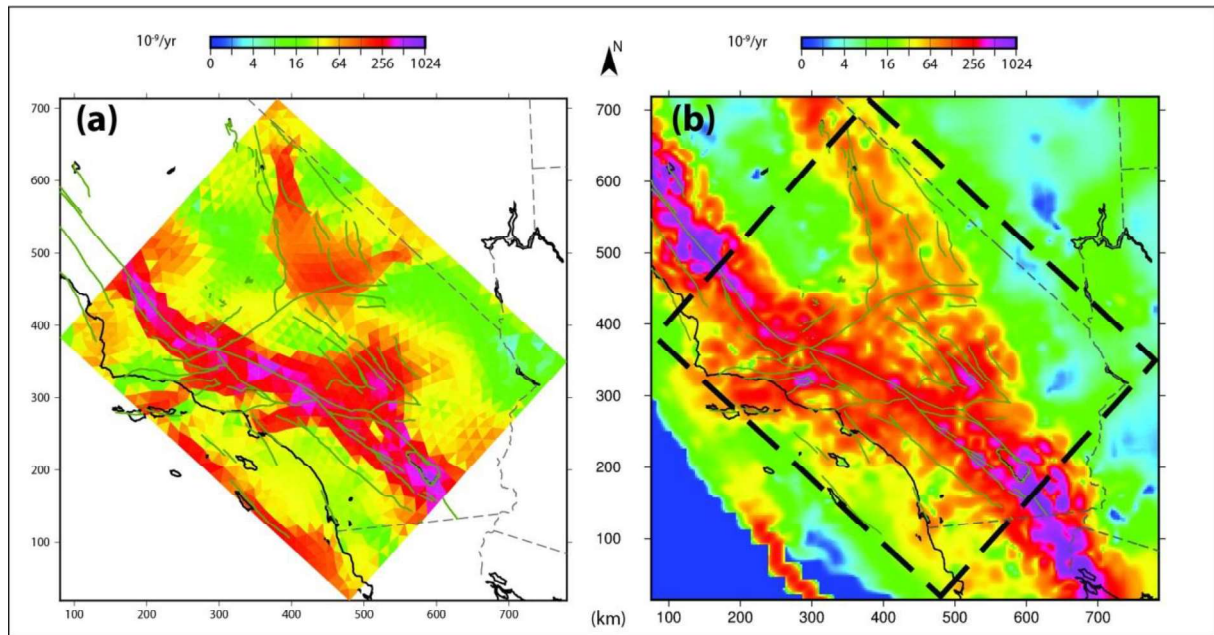


Fig. 11. Distribution of the strain rate for Zone 1. Second invariant of the strain rate tensor from (a) the upper (strongest) admissible values of our rigidity optimization and (b) the global strain map of Kreemer et al. (2014).

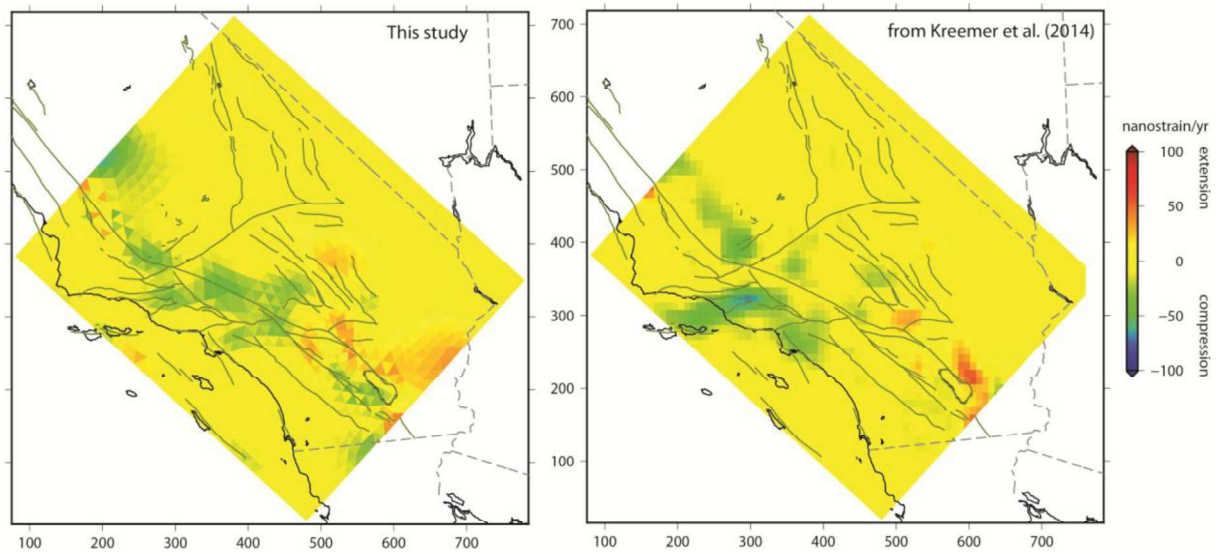


Fig. 12. Distribution of the first invariant of the strain rate tensor for Zone 1 from (a) our optimization and (b) the global strain map of Kreemer et al. (2014).

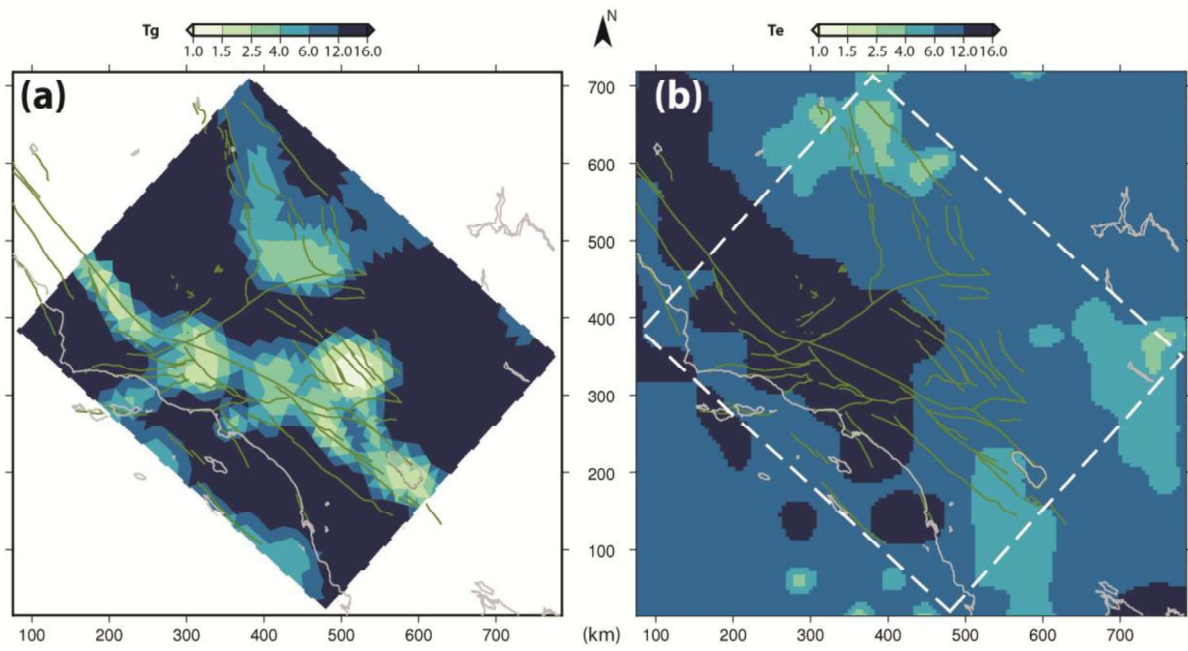


Fig. 13. (a) Geodetic elastic thickness T_g associated to our study; (b) flexural elastic thickness T_e given by Lowry and Pérez-Gussinyé (2011).

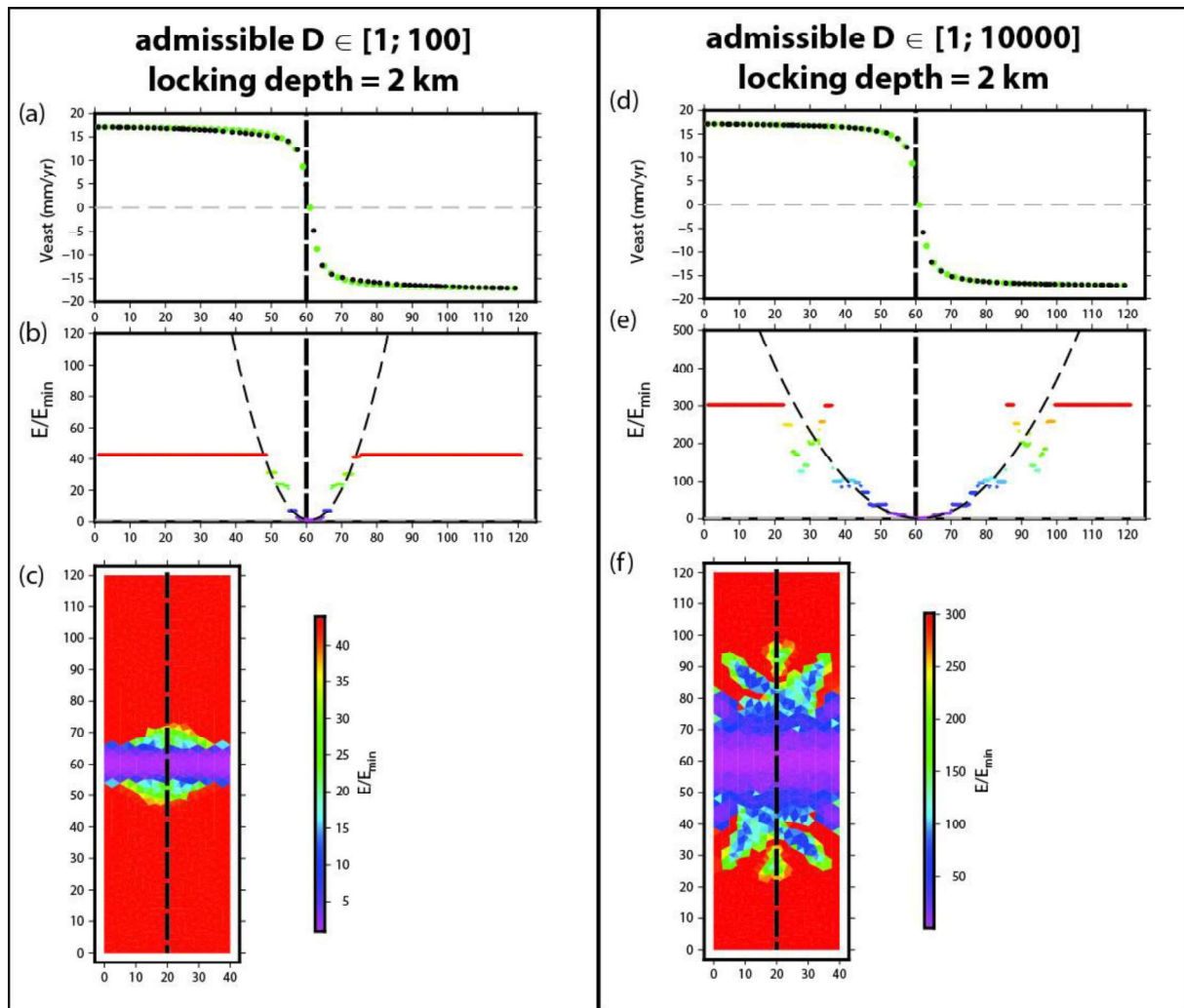


Figure A.1: Velocity and relative rigidity distributions for synthetic cases mimicking shallow creep on strike-slip faults. The locking depth is set to 2 km. The search interval for the relative rigidity has 2 orders (left) or 4 orders (right) of magnitude. (a and d) Theoretical velocities (green dots) and modelled velocities (black dots) at measurement locations along the profile (dotted black line) indicated in (c). (b and e) Theoretical (dashed curve) and modelled relative rigidity (colored dashes using same color palette as in (c) and (f) respectively) along the same profile. (c and f) Spatial distribution of relative rigidity determined by our inversion.

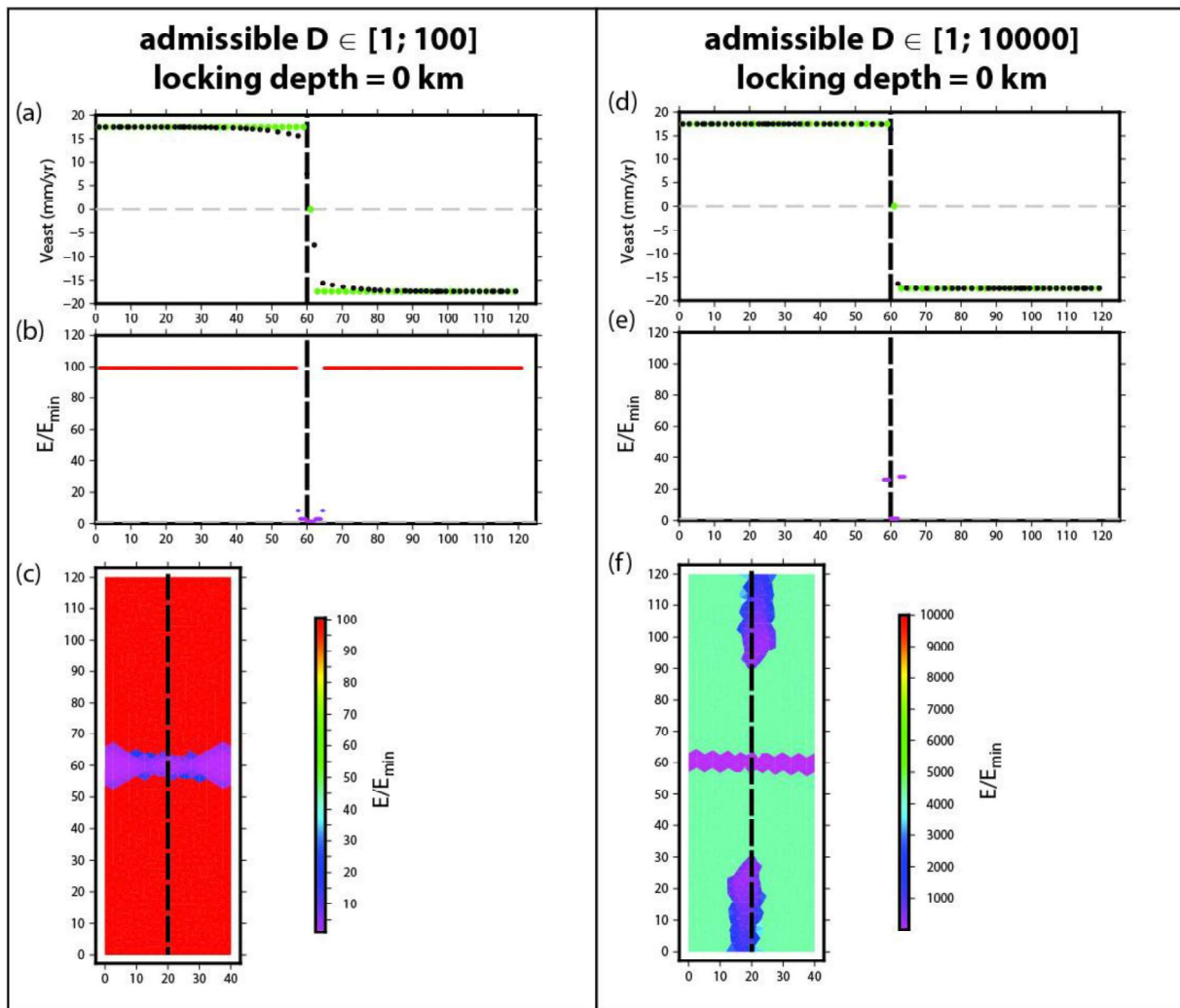


Figure A.2: Same as Fig. A.1 but the locking depth is now set to 0 km.

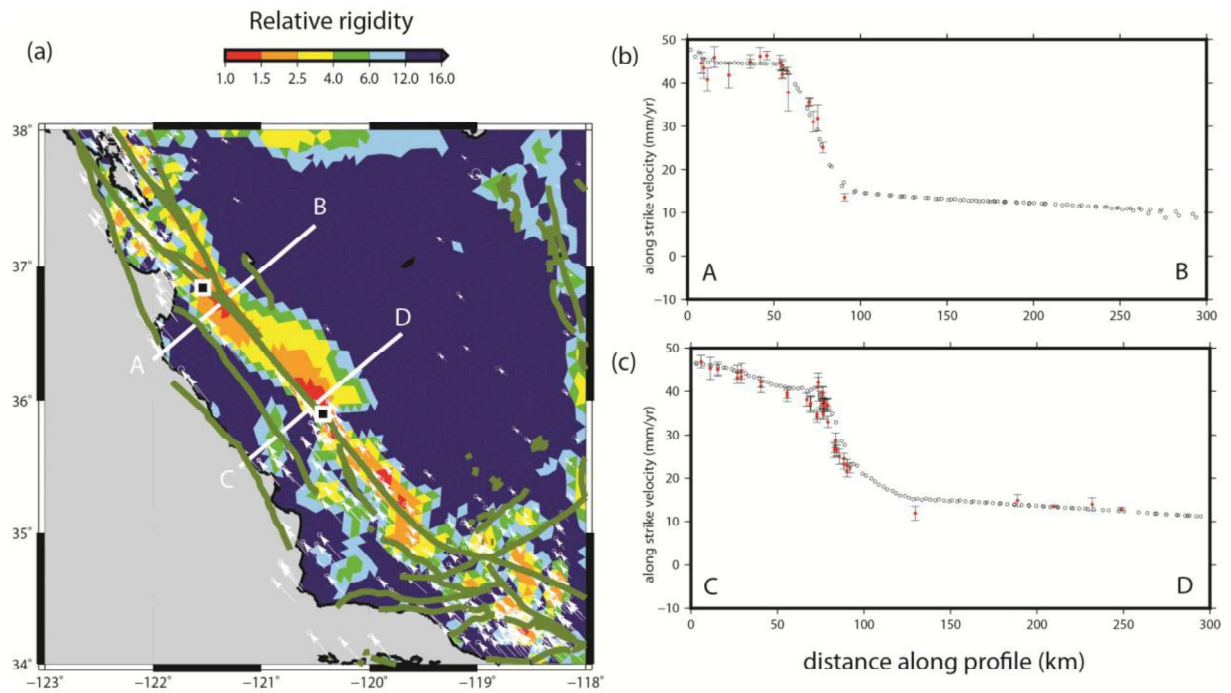


Figure A.2: (a) Relative rigidity distribution over the Parkfield segment of the SAF. Black squares indicate the location of the cities of San Juan Bautista (north) and Parkfield (south). White arrows are the velocities of the CMM3 database. Measured (red circles) and modelled (black circles) along-strike velocities along (b) A-B and (c) C-D profiles shown in (a).

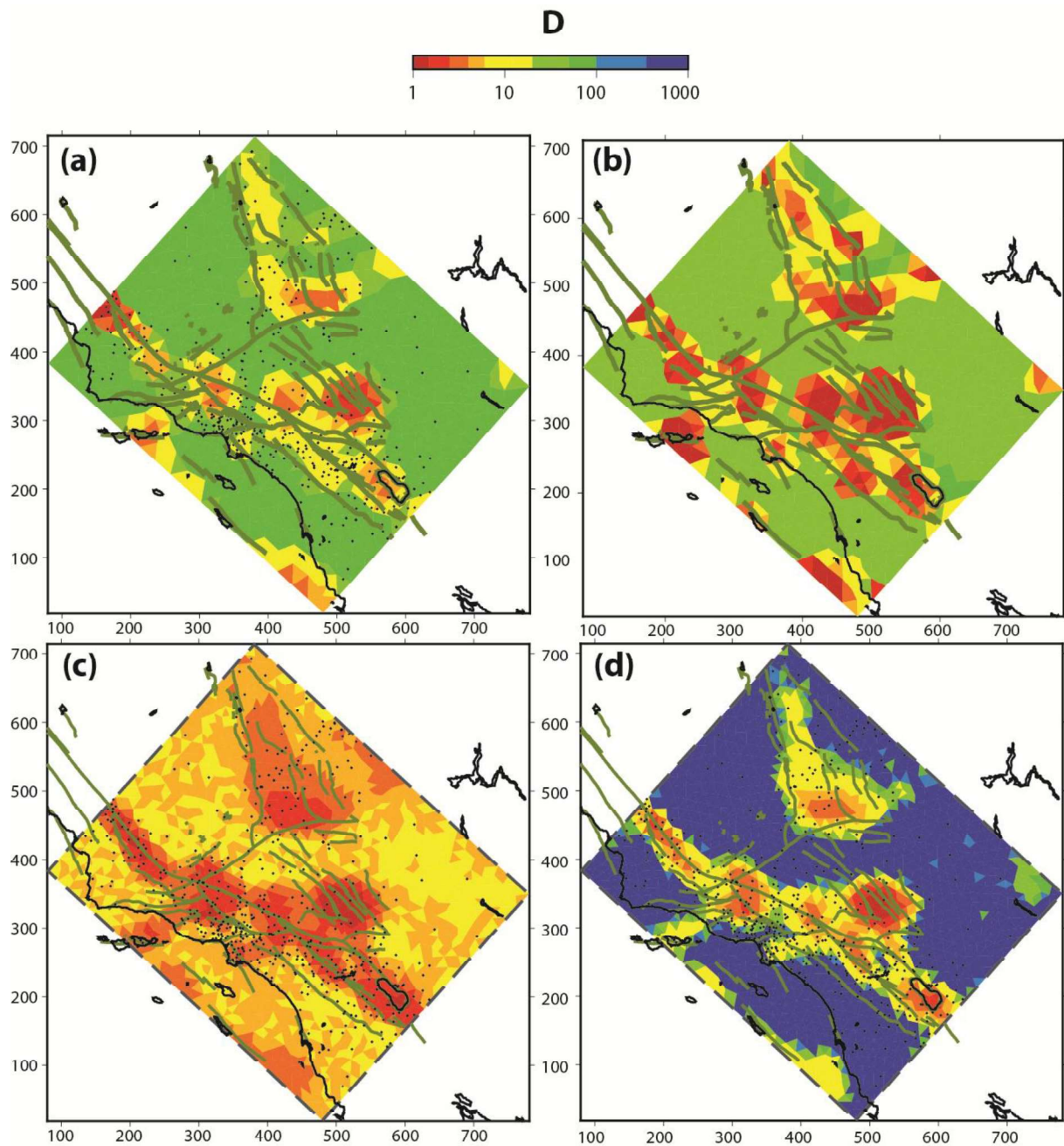


Figure B1: Rigidity distribution over Southern California as determined using a 4-order of magnitude range of admissible relative rigidity (from 1 to 10000). (a) Optimal solution, (b) Difference with respect to the optimal solution using a 2-order magnitude range (Fig. 8a) (c) lower bound solution and (d) upper bound solution. To be compared with Figures 8 and 9.